Corrigendum to ‘Structural analysis and fluid geochemistry as tools to assess the potential of the Tocomar geothermal system, Central

Geothermics 98 (2022) 102297

Contents lists available at ScienceDirect

Geothermics

journal homepage: www.elsevier.com/locate/geothermics

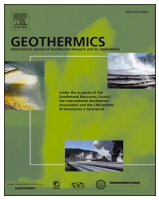

Structural analysis and fluid geochemistry as tools to assess the potential of the Tocomar geothermal system, Central Puna (Argentina)

Rubén Filipovich [a,*], Agostina Chiodi [a], Walter Báez [a], Maria Florencia Ahumada [b], Chiara Invernizzi [c], Sara Taviani [d], Luca Aldega [e], Franco Tassi [f], Alfonso Barrios [g], Sveva Corrado [h], Gianluca Groppelli [i], Gianluca Norini [i], Sabina Bigi [e], Chiara Caricchi [j], Arnaldo De Benedetti [g], Gianfilippo De Astis [j], Raúl Becchio [a], José Germán Viramonte [a], Guido Giordano [h]

[a] *Instituto de Bio y Geociencias del NOA (IBIGEO, UNSa-CONICET), Av. 9 de Julio 14, A4405BBA Salta, Argentina*
[b] *Instituto Geofísico Sismológico Volponi (IGSV, UNSJ-CONICET), Km 12, RP N° 12, Rivadavia, San Juan, Argentina*
[c] *Università di Camerino, Scuola di Scienze e Tecnologie – Sezione di Geologia, Via Gentile III da Varano, 7 - 62032 Camerino (MC), Italy*
[d] *Department of Earth and Environmental Sciences, University of Milano-Bicocca, Milan, Italy*
[e] *Sapienza Università di Roma, Dipartimento di Scienze della Terra, Piazzale Aldo Moro, 5, 00185 Rome, Italy*
[f] *Department of Earth Sciences, University of Florence, Via La Pira 4, 50121 Florence, Italy*
[g] *Deep Energy, Sanchez de Bustamante 447, C1173ABG Buenos Aires, Argentina*
[h] *Università degli Studi di Roma Tre, Dipartimento di Scienze, Largo S. L. Murialdo 1, 00146 Rome, Italy*
[i] *CNR-IGAG Istituto di Geologia Ambientale e Geoingegneria – sez. di Milano, Via M. Bianco 9, 20131 Milan, Italy*
[j] *Istituto Nazionale di Geofisica e Vulcanologia, 00143 Rome, Italy*

ARTICLE INFO

Keywords:
Southern Central Andes
Geothermal exploration
Conceptual model
Fault-related
Geothermal potential

ABSTRACT

The Argentinean Andean region hosts a vast geothermal resource clustered by active magmatic and tectonic activity. One of the most studied geothermal areas is the Tuzgle-Tocomar geothermal system in Central Puna (NW Argentina). However, despite the existence of several studies since the 1970′s highlighting the geothermal potential of the area, only highly schematic and dissimilar conceptual models have been proposed for the Tocomar Geothermal System. This study presents new detailed geological-structural and hydrogeochemical data, together with in-situ permeability analysis of fault zones and Raman spectroscopic characterization of hydrothermal-alteration minerals. The electrical generating capacity has also been evaluated using the volumetric method and a stochastic approach. A new comprehensive conceptual model of the studied area was constructed highlighting the role of the Calama-Olacapato-El Toro (COT) fault-system in the circulation of hydrothermal fluids. The reservoir of the Tocomar geothermal system has a Na^{+}-Cl^{-}(HCO_3)$^{-}$ composition and an estimated temperature of ~235 °C. Such a reservoir is hosted in fractured Ordovician rocks and controlled by the COT-like Chorrillos transpressive fault at 1000–1500 m depth b.g.l. The water isotopic data and hydrological features indicate a regional recharge beyond the Tocomar sub-basin boundaries (>5000 m a.s.l.). Additionally, the main hydrothermal reservoir receives inputs of magmatic fluids from the degassing of the intra-crustal rhyolitic magma chamber of the Tocomar volcanic center. The Monte Carlo simulations suggest that the Tocomar geothermal system has a probable power production capacity above 1.23 MWe (P90), 6.18 MWe (P50) and 11.67 MWe (P10) at different confidence levels. All calculations were biased towards minimum values, thus a tighter definition of the resource size and fracture porosity would significantly impact on the predictions. Notwithstanding, the strategic position of the Tocomar geothermal field encourages move forward towards more in-depth exploration phases.

* Correspomding author.
E-mail address: rubenfilipovich@yahoo.com.ar (R. Filipovich).

https://doi.org/10.1016/j.geothermics.2021.102297
Received 8 June 2021; Received in revised form 19 August 2021; Accepted 11 November 2021
Available online 20 November 2021

1. Introduction

Volcanoes in subduction zones have associated nearly 75% of productive and prospective geothermal power plants worldwide (Moeck, 2014). Volcanic arcs include most of the existing Pleistocene and Holocene subaerial volcanoes on Earth, being these volcanoes substantial indicators of near-surface heat sources (Stelling et al., 2016). Vieira and Hamza (2019) estimated that the entire South American continent has a geothermal potential of about 5.226×10^{12} GJ (at depths not exceeding three kilometers), whereas the geothermal resource per unit area in the Andean region is >294 GJ/m^2. The Nazca-South America convergent margin involves promising sites for geothermal exploration marked by high heat flow (>110 mW/m^2) related to the Central and Southern volcanic zones (Springer and Förster, 1998; Lucazeau, 2019) (Fig. 1a). Nevertheless, only one geothermal plant (Cerro Pabellón, Chile) is currently producing electricity on a large-scale across the entire continent, making the Andes the largest undeveloped geothermal region in the world (Sanchez-Alfaro et al., 2015). Argentina has an estimated geothermal potential of 490 - 2010 MWe (Bona and Coviello, 2016), which is currently used for balneology (52.7 %), domestic use (24.6 %), home heating (4.6 %), greenhouses (4.5 %), aquaculture (1.5 %), industrial uses (6.7 %) and snow melt (5.4 %) (Chiodi et al., 2019). High-temperature geothermal systems (>230 °C; Sanyal, 2005) in Argentina are located in the western sector associated with the Neogene-Quaternary magmatic arc (Fig. 1a), whereas low-temperature geothermal systems (<150 °C; Sanyal, 2005) associated with deep circulation of meteoric waters occur toward the east (extra-Andean region) (Fig. 1b). Barcelona et al. (2017) suggested that the region with the highest geothermal potential in Argentina is located in the Andean Southern Volcanic Zone (SVZ, 33–46° S) due to its tectonic and volcanic features (Fig. 1a). Toward the North, within the Central Volcanic Zone (CVZ, 16–28° S; Fig. 1a), the geothermal projects at the most advanced exploration stages are within the formerly called Tuzgle-Tocomar geothermal area (e.g. Aquater, 1980; Hidroproyectos et al., 1984; CREGEN, 1988; Giordano et al., 2013) (Fig. 1b). However, Coira (2008) and Giordano et al. (2016), based on hydrochemical compositions, revealed the existence of two independent geothermal systems proposing a preliminary conceptual model for the Tocomar Geothermal System (TGS).

The TGS is located in the Central Puna (~24° S, NW Argentina) related to the Tocomar volcanic field (Petrinovic and Colombo Piñol, 2006; Petrinovic et al., 2006) emplaced in a small extensional basin the "Tocomar basin", linked to the active NW–SE trending left-lateral strike-slip Calama–Olacapato– El Toro (COT) fault system (Petrinovic and Colombo Piñol, 2006; Giordano et al., 2013, 2016) (Fig. 1c). The TGS has been considered as a planar structure with no development of deep reservoirs (Coira, 2008) favoured by the COT-related vertical permeability enhancement (Giordano et al., 2013, 2016). These studies have been mainly focused on the hydrothermal circulation and do not fully explain the relationship between the components of the geothermal system, reservoir geometry and fluid chemistry. On the other hand, the TGS is potentially very interesting as a geothermal prospect as it is

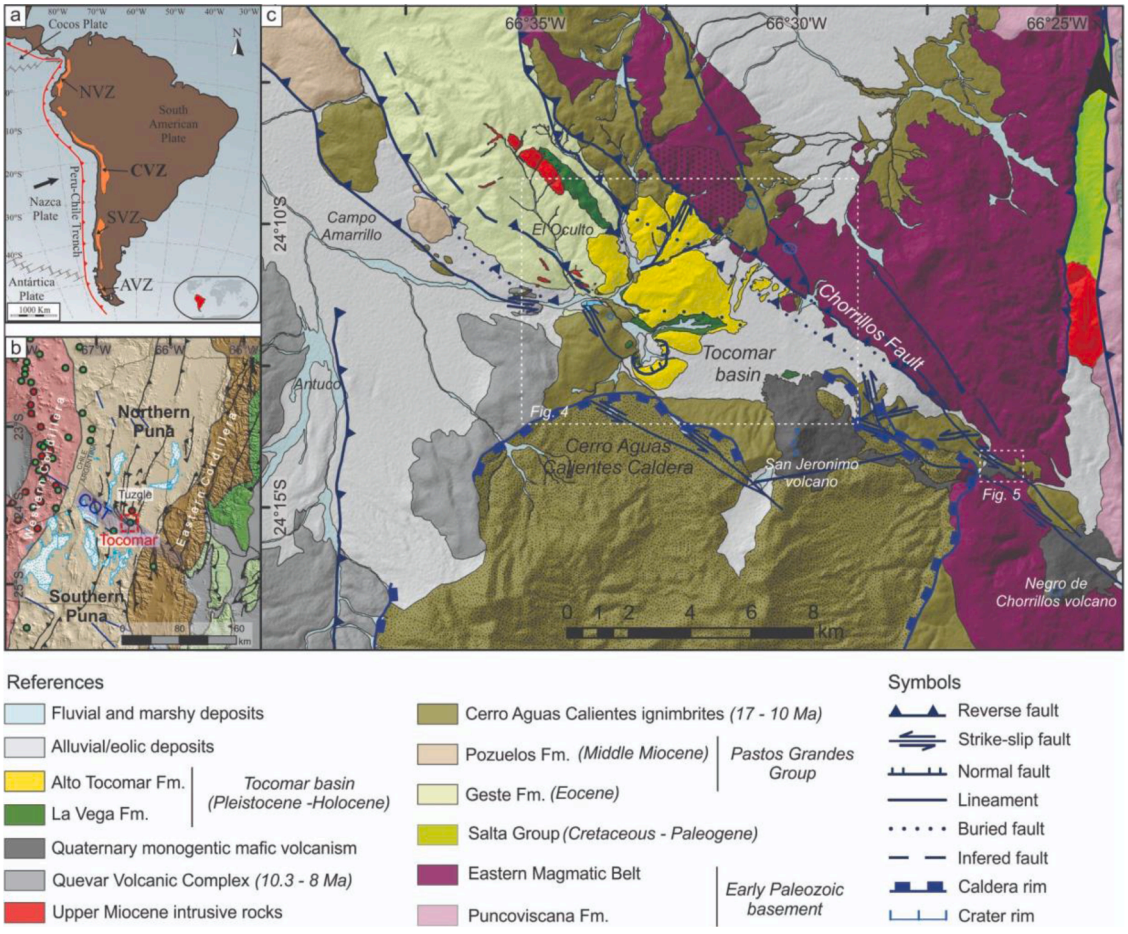

Fig. 1. (a) Distribution and extension of the main Andean volcanic zones. Northern volcanic zone (NVZ); Central volcanic zone (CVZ); Southern volcanic zone (SVZ); Austral volcanic zone (AVZ). (b) Major morphostructural units from NW Argentina and tectonic framework of the Puna plateau. Pleistocene (green dots) and Holocene (red dots) volcanoes are also shown (database from Smithsonian Institution Global Volcanism Program). In blue the COT (Calama - Olacapato - El Toro) fault system domain. The location of Fig. 1c is shown by a red square. (c) Geological setting of the Tocomar geothermal area (modified from Filipovich et al., 2020). Insets show the location of Figs. 4 and 5 (For interpretation of the references to color in this figure legend, the reader is referred to the web version of this article).

crossed by the bioceanic corridor made by the national route 51, by the Belgrano railway, by gas pipeline and by the high-voltage (HV) power transmission line (345 kV) connecting Chile and Argentina. In addition, this HV power transmission line integrates 300 MW into the grid, from a photovoltaic project (Puna Solar) 20 km west (Fig. 2). Additionally, the TGS is surrounded by numerous mining Cu-Au prospects, lithium projects and plants, and scientific-technological projects (Fig. 2). We propose referring to this area in the future as the Central Puna Energy Hub (CPEH).

The construction of an accurate conceptual model of the TGS is challenging due to its complex geological-structural framework. However, previous background, its geothermic potential and its strategic location merit advancing in its knowledge and characterization. The present paper reports and discusses the results of a detailed geological-structural and geochemical survey carried out in the Tocomar geothermal area with the aims to: i) identify the lithological units that acts as reservoir and seal of the geothermal system, ii) define the structures that confine the reservoir as well as structures that acts as fluid pathways, iii) establish the physicochemical conditions of the fluids into the reservoir and the secondary processes that control their chemistry as well as to define the primary source of the fluids. Finally, a novel conceptual model of the TGS with an estimation of the geothermal potential is proposed.

2. Geodynamic and geological setting

One of the most outstanding topographic features of the Central Andes (15°-34° S; Tassara, 2005) (Fig. 1a) is the development of the Andean plateau or Altiplano-Puna (Isacks, 1988). This continental-scale feature constitutes a paradox in plate tectonics since it is the second highest plateau in the world, after the Tibet plateau, associated with a non-collisional environment (Allmendinger et al., 1997), a unique feature in the most 60,000 km of convergent boundaries (Oncken et al., 2006). The plateau is characterized by the presence of endorheic basins, salt flats, active tectonics and voluminous and extensive ignimbrites sheets (Jordan, 1983; Isacks, 1988; Allmendinger et al., 1997; Sobolev and Babeyko, 2005) related, mainly, to the Altiplano Puna Volcanic Complex (APVC, de Silva et al., 1989). The Puna (NW Argentina; Fig. 1b), constitutes the southern sector of the plateau with a mean elevation of 4400 m a.s.l. associated with a thickened crust (Whitman et al., 1996). Several models have been invoked to explain the unusual thick crust and uplift of the Puna plateau (e.g. Garzione et al., 2017). Some studies have argued that the initial growth phase of the Puna took place 40 Ma ago and the deformation would have continued diachronous and spatially distributed throughout the Neogene (e.g. Cladouhos et al., 1994; Marrett et al., 1994; Marrett and Strecker, 2000; Coutand et al., 2001; Hongn et al., 2007; Strecker et al., 2007, 2012; Garzione et al., 2008; del Papa et al., 2013) but always in a continuous evolution (Barnes and Ehlers, 2009).

In the study area, the basement consists mainly of highly deformed meta-pelites and meta-arenites of the late Neoproterozoic to early Cambrian Puncoviscana Formation (Turner, 1964; Aceñolaza and Aceñolaza, 2005) covered by a Lower Paleozoic volcano–sedimentary succession (Blasco et al., 1996; Aceñolaza et al., 1999; Sánchez and Salfity, 1999; Norini et al., 2013) (Fig. 1c). These polydeformed units are intruded by meta-granitoid rocks of the Eastern Magmatic Belt (Suzaño et al., 2017) and unconformably covered by the Cretaceous–Paleocene syn- and post-rift sedimentary sequence of the Salta Group and the Tertiary siliciclastic and evaporitic deposits of the Pastos Grandes Group (Fig. 1c) related to the Andean broken foreland basin evolution (Turner, 1960, 1964; Schwab and Lippolt, 1974; Koukharsky and Munizga, 1990; Alonso, 1992; Blasco et al., 1996; Hongn et al., 2007; Carrapa and DeCelles, 2008). Volcanic activity produced Miocene-Quaternary dacitic to rhyolitic pyroclastic deposits and domes (Petrinovic and Colombo Piñol, 2006; Riller et al., 2001; Petrinovic et al., 2005; 2006; 2010; Báez et al., 2018), and monogenetic basaltic centres (Déruelle, 1991; Coira and Kay 1993; Kay et al., 1994; Norini et al., 2014; Seggiaro et al., 2016) (Fig. 1c).

At the Central Puna, the protracted and superimposed tectonic events result in a complex structural grain characterized by both orogen-parallel double-vergent reverse fault systems and folds as well as by orogen-oblique faults systems that accommodate the general compressive regime (Blasco et al., 1996; Coutand et al., 2001; Hongn et al., 2010) (Fig. 1b). The roughly N-S trending reverse faults show

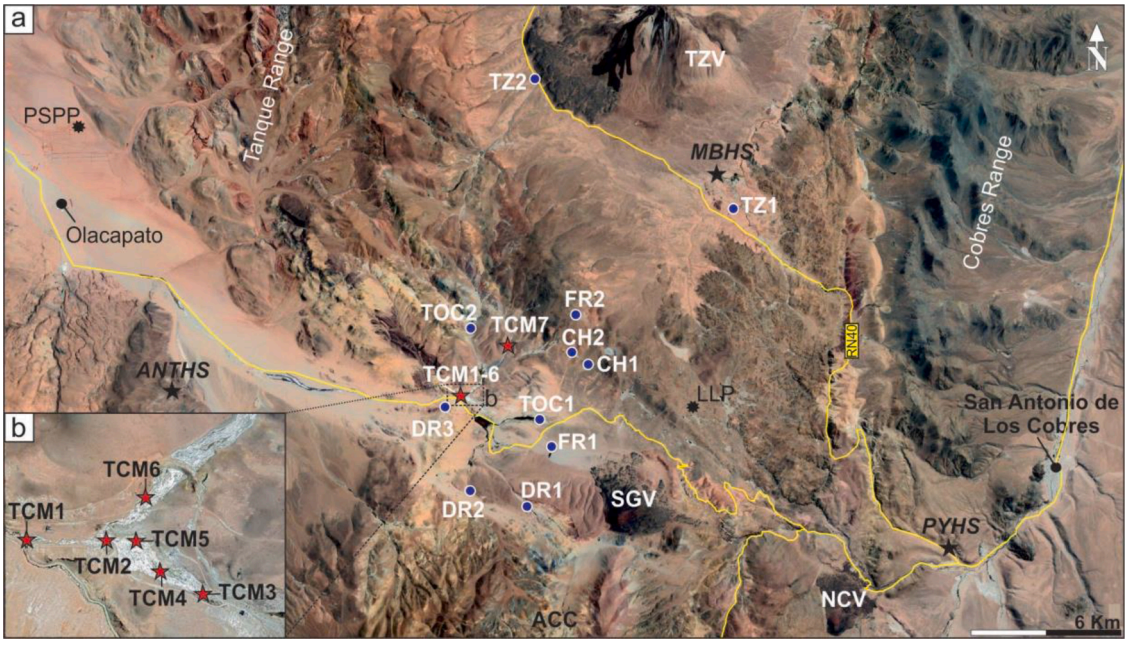

Fig. 2. (a) Satellite image (Google Earth data) of the study area with the location of the sampling sites, (b) Enlargement of the Tocomar hot springs main area. Red stars: sample location (hot spring). Blue circles: sample location for stream/cold spring. ANTHS: Antuco hot springs. MBHS: Mina Betty hot springs. PYHS: Pompeya hot springs. ACC: Aguas Calientes caldera. TZV: Tuzgle volcano. SGV: San Gerónimo volcano. NCV: Negro de Chorillos volcano. PSPP: Puna Solar Photovoltaic project. LLP: LLAMA Astronomic Project (For interpretation of the references to color in this figure legend, the reader is referred to the web version of this article).

along-strike variations and juxtapose Precambrian-Ordovician units over Cretaceous-Recent continental sediments and volcanic rocks, deflected or interrupted by NW-striking lineaments (Viramonte et al., 1984; Salfity et al., 1985; Blasco et al., 1996; Allmendinger et al., 1997) (Fig. 1b). The most prominent transverse lineament in the region is the active left-lateral transcurrent COT fault system (Fig. 1b) developed as a transfer zone among the main N-striking thrusts (Riller et al., 2001; Petrinovic et al., 2010) that evolved as part of the same tectonic system accommodating the crustal E-W shortening since the Miocene (Acocella et al., 2011; Norini et al., 2013). The COT system consists of several WNW- to NW-trending primary fault strands (Seggiaro, 2006) and minor ENE-WSW secondary normal and strike-slip faults (Petrinovic et al., 2005; 2006; Giordano et al., 2013; Lanza et al., 2013; Norini et al., 2013; Seggiaro et al., 2017). The COT-related intense deformation would have weakened the crust and led to the emplacement of the Mio-Pleistocene Quevar transversal volcanic chain (Viramonte et al., 1984; Petrinovic et al., 1999; 2010; Riller et al., 2001; Matteini et al., 2002; Ramelow et al., 2006; Acocella et al., 2011).

The anomalous heat-flow across the Central Puna (>160 mW/m^2; Ibarra and Prezzi, 2019), given by a complex distribution of magma/-fluid reservoirs (<5–8 km; Schwarz et al., 1994; Lezaeta and Brasse, 2001; Schurr et al., 2003; Petrinovic et al., 2006; Araya-Vargas et al., 2019; Ibarra and Prezzi, 2019) and recent active tectonics (e.g. Norini et al., 2013), favored the discharge of numerous fossil and active thermal springs aligned along the COT system such as Antuco, Tocomar and Pompeya springs (Fig. 2a).

3. Tocomar basin: geological and geothermal background

The TGS is located in the Central Puna (Southern Central Andes, NW Argentina; Fig. 1b) related to the <0.57 Ma Tocomar volcanic center (TVC; Petrinovic et al., 1999; Petrinovic and Colombo Piñol, 2006) emplaced in the Tocomar basin linked to the active COT fault system (Fig. 1c). This small rhomboidal (~30 km^2) fault-bounded basin developed onto an articulated substratum that includes i) Ordovician granitoids from the Eastern Magmatic Belt (Suzaño et al., 2017) exposed along the NW-trending Chorrillos high (Fig. 1c), ii) Middle Eocene foreland-related deposits of the Geste Formation (Alonso, 1992; Carrapa and DeCelles, 2008) (Fig. 1c) and iii) Miocene ignimbrites from the Cerro Aguas Calientes Caldera (CACC; Petrinovic et al., 2010) (Fig. 1c). The basin infill consists of shoshonitic lava flows of the Cerro San Jerónimo with ages from 0.78 Ma (Aquater, 1979) to 0.144 Ma (Fernandez-Turiel et al., 2021) and Pleistocene fluvial/alluvial sediments (La Vega Formation; Filipovich et al., 2020) covered by a complex sequence of pyroclastic deposits from the Alto Tocomar Formation (Filipovich et al., 2020). Volcanic products from TVC are mainly rhyolitic in composition (Petrinovic et al., 2005; 2006; Petrinovic and Colombo Piñol, 2006) with ages ranging from 1.15±0.3 Ma (Aquater, 1980) to 0.55±0.1 Ma (Petrinovic et al., 1999). The structural style of the study area is the result of the complex interaction between orogen-parallel thrusts and orogen-oblique COT fault system (Fig 1c). The most important structural feature is the active NW-striking transpressive left-lateral Chorrillos fault (CF) that thrusts the Ordovician basement rocks, structuring the Chorrillos high (NE boundary of the Tocomar basin), over continental Tertiary sediments and Miocene volcanic units (Fig. 1c). Internally, extensional, transcurrent and reverse faults affect the Quaternary deposits suggesting an extensional origin (Petrinovic et al., 2006; Giordano et al., 2013). However, the basin origin still remains unclear (e.g. Filipovich et al., 2020). This local extensional component of motion has been thought as the key factor for the enhanced magma storage and fluid circulation (Petrinovic and Colombo Piñol, 2006; Petrinovic et al., 2006; Acocella et al., 2011; Giordano et al., 2013; 2016).

The area forms part of the larger Puna plateau intermontane hydrologically closed system, where surface waters flow toward endorheic depressions that form salar for evaporation (e.g. Sobel et al., 2003; Warren, 2010; García et al., 2020). It is characterized by a very dry climate with an average rainfall lower than 115 mm per year that is distributed from December to March and an average annual temperature of 7.2 °C (Bianchi et al., 2005; Sanci et al., 2020 and references therein). Such a low precipitation rate causes a significant water deficit all year (annual deficit ~367 mm; Sanci et al., 2020). Due to the very low availability of rainwater in the area, the rivers, which normally have a permanent regime, are mostly associated with hot springs in their headwaters (Moya Ruiz, 1993; Paoli, 2003; Giordano et al., 2013, 2016). The TGS is represented at surface by several hot springs with temperature up to 70.2 °C distributed in a small area (<0.4 km^2) along with Middle-Upper Pleistocene travertine deposits (<160 ka; Filipovich et al., 2020). Additionally, the Tocomar area shows evidence of hydrothermal alteration and sub-surface geothermal manifestations, such as phreatic and phreatomagmatic craters (Fig. 1c) related to the TVC activity (Petrinovic et al., 2006; Giordano et al., 2013; Filipovich et al., 2020).

Since 1970′s the vast majority of studies have focused on the Tuzgle geothermal prospect where multiple shallow temperature gradient wells were drilled thus completing the pre-feasibility stage (Coira, 1995, 2008). On the other hand, although several authors have highlighted the geothermal potential of the TGS (e.g. Coira 2008; Pesce, 2010; Giordano et al., 2013, 2016; Chiodi et al., 2019), a consistent model of the geothermal system has not been proposed yet. Based on geoelectric profiles interpretation and the hydrogeochemical data, Coira (2008) proposed a flow model through a vertical conductive structure without either development of horizons or continuous layers that could act as deep reservoirs or an effective and continuous seal layer. On the other hand, Giordano et al. (2013) proposed a “schematic” conceptual model, where the main reservoir is hosted within the Ordovician basement, across a main fault zone, at medium to high enthalpy conditions (~120 - 227 °C) with a heat source related to the volcanism of TVC (Giordano et al., 2016). Although there is a preliminary knowledge about overall characteristics of the shallow manifestations as well as geological context of TGS, the available information shows that this geothermal system is the most promising in the Central Puna (Giordano et al., 2013; Lindsey et al., 2021).

4. Methods

4.1. Field analysis and sampling

For this study, a holistic approach has been applied integrating available geological maps (e.g. Blasco et al., 1996; Petrinovic et al., 2010; Bonali et al., 2012; Giordano et al., 2013; Filipovich et al., 2020), published volcanological and structural data (e.g. Marrett et al., 1994; Petrinovic et al., 2005; 2006; Bonali et al., 2012; Lanza et al., 2013; Norini et al., 2013), hydrologic and geochemical surveys (e.g. Moya Ruiz, 1993; Bianchi et al., 2005; Paoli, 2003; Sanci et al., 2020), remote sensing, and field-based analysis at different scales in order to identify the main and secondary tectonic structures.

4.1.1. Fracture analysis and mineralogy of the deuteric products

Qualitative and quantitative characterization of fractures was performed on both basement and Tocomar basin units. In the field, geometrical features, such as trace length and orientation, distribution, displacement, infill material, and also type and mode of deformation associated with fractures were analyzed. Structural data were statistically analyzed by Gaussian fitting automated techniques in order to detect different populations of fractures as well as the mean and standard deviation values (Salvini et al., 1999).

Close to the main geothermal springs (Fig. 2b), seven altered rocks samples were collected to determine the mineralogy of the deuteric products by Raman analysis. Crystals were randomly oriented and the Thermo Almega micro-Raman system was set at 100% power, using a 532 nm solid-state laser and a thermoelectrically cooled CCD detector. The laser was partially polarized with 4 cm-1 resolution and a spot size

of 1 μm. Search-match was performed with Thermo Almega Omnic and CrystalSleuth software. Trimming and background removal were performed by CrystalSleuth software.

4.1.2. Fault zone analysis and in-situ permeability measurements

Currently, there is no detailed information that allows defining and delimiting the fault zone related to the COT. The understanding of the internal structure of large-displacement strike-slip fault zones, such as COT (>15 km; Allmendinger et al., 1983), is challenging since deformation tends to distribute over wide deformation zones rather than along discrete planes, cutting through rocks of different lithologies (e.g. Faulkner et al., 2003, 2008). For this purpose, on the trace of the COT fault system, representative outcrops were selected for fault zone characterization considering: fault architectural elements, fracture patterns and fault rocks (e.g. Sibson, 1986; Caine et al., 1996; Faulkner et al., 2003, 2010). In the Tocomar area, the left-lateral transpressive CF is the best well-defined COT segment. On the most complex and complete outcrop of the CF zone (CFZ; Fig. 1), in-situ permeability measurements were performed by using a mini-field permeameter (Tiny-Perm II). The measurements were carried out on fault planes, protoliths, and fault rocks. According to the grain size of the sampled material, an average of 5 to 15 measurements were taken per sampling point in order to obtain a representative value. The Tiny perm II air minipermeameter provides reliable permeability measurements in the range of 10^{-3} - 10^{1} Darcy.

4.2. Fluid sampling, hydrogeological measurements and analytical methods

4.2.1. Water and gas sampling

Eighteen water samples from 7 hot springs (TCM1, TCM2, TCM3, TCM4, TCM5, TCM6 and TCM7), 7 cold springs (TOC1, TOC2, CH1, CH2, DR1, DR2 and DR3), 2 creeks (TZ1 and TZ2) and 2 cold water lagoons (FR1 and FR2) were collected. Water temperature, pH and electrical conductivity were measured in the field using portable instruments (Hanna HI 98195; accuracy: ±0.15 °C, ±0.02 and ±1 %, respectively). Alkalinity (expressed as HCO_3^-) and silica were analyzed in situ by (i) acidimetric titration using HCl 0.03 N, phenolphthalein and bromophenol blue as indicators, and (ii) molecular spectrophotometry (Hanna HI 96770C; ±1 mg/L), respectively (Table 1). Water was sampled in high-density polyethylene bottles, as follows: 2 filtered samples at 0.45 μm and acidified with ultrapure HCl and HNO_3 for the analysis of major cations and trace elements, respectively, 1 filtered sample for the analysis of anions and 1 unfiltered sample for the analysis of water isotopes.

Bubbling gasses from TCM1, TCM2, TCM3, TCM4, TCM5, and TCM6 were sampled using a plastic funnel up-side-down positioned above the bubbles and connected through tygon tubes to the sampling flasks. The latter consisted of (i) a pre-evacuated 60 mL glass thorion tapped bottle filled with 20 mL of a 4 N NaOH solution for the analysis of the gas chemical composition (Giggenbach and Goguel, 1989) and (ii) a pre-evacuated 60 mL glass flask for the analysis of the carbon isotopic ratio in CO_2 (Vaselli et al., 2006).

Coordinates of sampling sites are reported in Tables 1 and 3 and plotted in Fig. 2.

4.2.2. Hydrogeological measurements

Hydrogeological surveys were performed at the end of the dry season (November 2014) and at the end of the wet season (April 2015). Flow rate measurements were carried out along transverse sections to the outflow direction in selected points, using a digital water velocity meter (*OCT C2*, accuracy ±2% m/s). Catchment areas were identified by combining digital elevation models (ALOS PALSAR DEM, 12 m), together with the isotopic data of water samples.

4.2.3. Chemical and isotopic analyses of water samples

Major cations (Na^+, K^+, Ca^{2+}, Mg^{2+}, Li^+ and NH_4^+) and anions (F^-, Cl^- SO_4^{2-}, Br^- and NO_3^-) were analyzed by ion-chromatography (IC: Metrohm 861 and 761, respectively). The analytical error is ≤5 %. Boron was analyzed by molecular spectrophotometry (MS; Beckman DU 520) using the Azomethine-H method (Bencini, 1985). The analytical error is ≤5 %.

Trace elements were analyzed by Inductively Coupled Plasma Optical Emission Spectrometry (ICP-OES) using an Optima 8000 Perkin Elmer spectrometer. The analytical error is ≤10 %.

The $^{18}O/^{16}O$ and $^{2}H/^{1}H$ ratios in water (expressed as $\delta^{18}O–H_2O$ and $\delta^{2}H\text{-}H_2O$ ‰ vs. V-SMOW, respectively) were analyzed using an Ultra High-Precision Isotopic Water Analyzer *Picarro L2130-i* laser spectrometer. The analytical errors for $\delta^{18}O–H_2O$ and $\delta^{2}H–H_2O$ values are ±0.25 ‰ and ±1.20 ‰, respectively.

4.2.4. Chemical and isotopic analysis of dissolved and bubbling gasses

Inorganic gasses (N_2, O_2, H_2, CO, Ar, Ne and He) in the headspace of the soda flasks were analyzed by gas chromatography (GC) using a Shimadzu 15A instrument equipped with a Thermal Conductivity Detector (TCD). Carbon dioxide and H_2S in the alkaline solution were analyzed as CO_3^{2-}, by acidimetric titration with a HCl 0.1 N solution, and SO_4^{2-}, by IC after oxidation with H_2O_2, respectively. Methane and light hydrocarbons were determined by using a Shimadzu 14A gas chromatograph (GC), equipped with a 10-m-long stainless-steel column packed with Chromosorb PAW 80/100 mesh coated with 23% SP 1700 and a Flame Ionization Detector (FID). The analytical errors for GC analyses were ≤ 5%.

$^{13}C/^{12}C$ ratios of CO_2 (expressed as $\delta^{13}C\text{-}CO_2$ ‰ vs. V-PDB) was measured by using a Finningan Delta Plus mass spectrometer after standard extraction and purification procedures of the gas mixtures (Evans et al., 1998; Vaselli et al., 2006). Carrara and San Vincenzo marbles (Internal), as well as NBS18 and NBS19 (International) standards were used to estimate the external precision. The analytical errors were ±0.05‰ and ±0.1‰, respectively.

The $\delta^{13}C$ values of CH_4 from bubbling gasses were analysed by mass spectrometry (Varian MAT 250), following the procedure proposed by Schoell (1980). The analytical uncertainty was ± 0.15‰. In the dissolved gasses, the CH_4 concentrations were too low to allow any analysis of $\delta^{13}C\text{-}CH_4$.

Helium isotopic ratios (expressed as R/Ra, where R is the $^3He/^4He$ measured ratio and Ra is the $^3He/^4He$ ratio in the air: 1.39×10^{-6}; Mamyrin and Tolstikhin, 1984) and those of $^4He/^{20}Ne$ were determined by using a double collector mass spectrometer (VG 5400-TFT) according to the method described by Inguaggiato and Rizzo (2004). The analytical error was ±1 %. The R/Ra values were corrected for atmospheric contamination using the $^4He/^{20}Ne$ ratios (Poreda and Craig, 1989), as follows:

$$Rc / Ra = [(R / Ra_{measured}) - r]/(1 - - r) \quad (1)$$

where r is $(^4He/^{20}Ne)_{air}$ / $(^4He/^{20}Ne)_{measured}$ and that of $(^4He/^{20}Ne)_{air}$ is 0.421 at the estimated altitude of recharge of approximately 4000 m (Hoke et al., 1994).

5. Results

5.1. Structural field data

5.1.1. Measured faults and fractures system

The Tocomar basin is bounded to the west by west- and east-verging reverse faults cutting Tertiary strata (Fig. 1c). These tectonic structures change southward into left-lateral reverse oblique slip faults as it bends and merges with the COT fault system (Fig. 1c). This is evident southward of the El Oculto area where a northeast-dipping, NNW-striking left-reverse oblique slip fault repeats deposits of the Geste Formation and bends second-order folds that strike sub-parallel to the fault (Fig. 3a). At the outcrop scale, secondary faults as well as tension gashes and Riedel

Table 1
Chemical and stable isotopic ($\delta^{18}O$-H_2O and δ_D-H_2O in ‰ vs. V-SMOW) composition of cold and thermal waters from the Tocomar Geothermal System, Puna, Argentina. Concentrations are in mg/L. Geographic coordinates, altitude (A: m a.s.l.), pH values, outlet temperature (°C), EC: electrical conductivity (mS/cm), and TDS: Total Dissolved Solids (mg/L) are also reported. HS: hot spring, C: creek, CW: cold water, CS: cold spring. n.a.: not analyzed. CI: ionic charge imbalance.

ID	Type	Latitude	Longitude	A	T	pH	EC	HCO_3^-	F^-	Cl^-	Br^-	SO_4^{2-}	Ca^{2+}	Mg^{2+}	Na^+	K^+	NH_4^+	Li^+	H_3BO_3	SiO_2	TDS	$\delta^{18}O$	δ_D	CI %
TCM1	hot spring	24.186486° S	66.561225° W	4296	52.3	6.42	4.2	827	4.7	900	0.52	217	37	6.5	952	98	6.5	12	n.a.	n.a.	3151	-9.5	-81.5	5.05
TCM2	hot spring	24.186528° S	66.557750° W	4314	44.1	6.09	4	751	4.30	900	0.69	222	35	2.6	923	87	4.9	12	n.a.	160	3103	-9.6	-82.8	4.24
TCM3	hot spring	24.188528° S	66.553222° W	4348	38.8	6.87	4.11	824	4.2	906	0.56	217	44	5	924	91	4.4	12	n.a.	n.a.	3035	-9.0	-80.9	3.52
TCM4	hot spring	24.187861° S	66.554694° W	4337	70.2	6.51	4.1	769	4.7	879	0.52	212	34	5	854	78	5.9	11	n.a.	141	2995	-9.6	-81.3	1.31
TCM5	hot spring	24.186694° S	66.556000° W	4316	30.3	5.84	3.76	776	4.3	852	0.45	207	33	4	892	84	6.3	11	n.a.	n.a.	2871	-10.2	-84.2	4.19
TCM6	hot spring	24.184861° S	66.555833° W	4118	47.2	6.43	3.61	732	n.a.	624	n.a.	244	46	6	742	66	n.a.	7.16	44	n.a.	2511	-9.7	-82.0	4.32
TCM7	hot spring	24.166889° S	66.539556° W	4481	42.4	5.93	1.8	540	n.a.	266	n.a.	48	33	9	362	30	n.a.	4.02	28	n.a.	1320	-10.6	-81.7	4.25
TOC1	cold spring	24.193972° S	66.526667° W	4189	7.8	5.43	0.41	140	n.a.	13	n.a.	19	38	3	17	2	n.a.	n.a.	1	n.a.	233	-9.4	-73.1	-2.06
TOC2	cold spring	24.162667° S	66.554833° W	4434	17.8	7.3	1.15	321	n.a.	60	n.a.	125	57	37	69	5.7	n.a.	0.23	n.a.	n.a.	674	-7.0	-63.0	-2.89
TZ1	creek	24.124806° S	66.445500° W	4268	10	6.61	1.47	268	n.a.	281	n.a.	52	161	28	93	6	n.a.	n.a.	n.a.	n.a.	889	-6.6	-59.4	4.08
TZ2	creek	24.073028° S	66.526583° W	4347	20.1	6.36	0.45	162	n.a.	30	n.a.	19	35	9.4	35	7.8	n.a.	n.a.	n.a.	n.a.	297	-8.5	-64.7	4.13
FR1	cold water	24.204194° S	66.524278° W	4414	7.9	6.96	2.97	89	n.a.	159	n.a.	853	325	39.2	139	27	n.a.	n.a.	n.a.	n.a.	1631	2.5	-12.9	4.94
FR2	cold water	24.159000° S	66.513167° W	4711	6.8	7.24	4.67	211	n.a.	400	n.a.	2300	454	156	384	248	n.a.	n.a.	n.a.	n.a.	4153	-0.7	-24.3	-3.40
CH1	cold spring	24.171333° S	66.514944° W	4570	16.5	5.75	0.29	99	n.a.	13	n.a.	5	25	4.3	13	2	n.a.	n.a.	n.a.	n.a.	161	-8.4	-67.6	2.81
CH2	cold spring	24.174556° S	66.509611° W	4555	18.6	5.43	0.21	62	n.a.	8	n.a.	17	15	4.3	8	2	n.a.	n.a.	0.55	n.a.	117	-10.0	-76.6	-3.36
DR1	cold spring	24.226972° S	66.531111° W	4554	6.3	5.4	0.23	63	n.a.	7	n.a.	28	26	3.5	7	2	n.a.	n.a.	n.a.	n.a.	136	-9.7	-76.2	3.35
DR2	cold spring	24.220278° S	66.554750° W	4241	21.7	5.82	0.24	55	n.a.	6	n.a.	35	26	3.8	8	1	n.a.	n.a.	n.a.	n.a.	135	-9.6	-75.8	5.08
DR3	cold spring	24.191028° S	66.565528° W	4147	22.1	7.61	0.41	194	n.a.	14	n.a.	33	36	12.2	32	4.9	n.a.	0.33	0.85	n.a.	326	-9.6	-77.8	0.50

shears intersect the fault zone (Fig. 3a). This relationship suggests that both N-trending and COT-like structures are geometrically linked and evolved contemporaneously, as suggested by Norini et al. (2013). Towards the basin center, measured faults mostly strike N30°E to N60°E with en-echelon geometry and considerable dispersion (Fig. 3a). The data show variable kinematics including dip-slip normal (Fig. 3b) and reverse faults as well as dextral- and sinistral-oblique slip faults with normal and reverse components of displacement (Fig. 3c). The vertical throw of normal faults never exceeds 1 m and occurs as individual planes or forming conjugate fault sets (Fig. 3b). The fault zones exhibit synthetic (R) and antithetic (R') riedel shears, tension gashes (Fig. 3c), and discolored patches along fractures/fault planes (Fig. 3d). Further east, several overlapping parallel fault strands striking NW-SE and ENE-WSW delimit an intense deformation corridor mainly developed on basement rocks and CACC ignimbrites (Fig. 1c). This corridor is dominated by subvertical strike-slip faults whose kinematics varies from transpressive left- to right-lateral according to the main orientation of the planes (Fig. 3d) with deformation zones that range in width, according to the displacement of the faults and subsidiary fractures, from a few centimeters up to about >20 m (e.g. CF).

Along a 20 km long section, a total of 855 fractures were measured. From the statistical analysis of these fractures, 5 sets have been identified throughout the study area (Fig. 3a, inset). The statistically most significant fractures set have preferential orientation ranging from ~NE-SW (N60 ° E ± 10 °, Set I) to E-W (N90 ° E ± 10 °, Set II) and to a lesser extent NNW-SSE (Set IIIA) to NNE- SSW (Set IIIB). The less statistically significant fracture set is the ~N-S trending (Set IV) (Fig. 3a). The fracture dip is highly variable, but most have inclinations >70°.

5.1.2. Chorrillos fault zone structure and permeability

The CF consists, at least, of 3 well-defined subvertical main segments that strike NW to WNW cutting the Ordovician basement rocks, Miocene volcanic rocks, and Quaternary lava flows (Fig. 1c). Although, the fault plane is partially buried by the Quaternary basin fill to the northwest, the fault trace is marked by a 200 m high and ~12 km long scarp (i.e. Alto de Chorrillos; Fig. 1a) with several aligned cold springs at the base. In contrast, to the southeast the CF is well exposed and marked by NW- to WNW-trending fissures, sag ponds, linear ridges, and metric- to decametric-scale fault scarps that affect Quaternary mafic lavas (Fig. 1c). Fig. 4a shows that the exposed CFZ is, at least, ~21 m wide and consists of subparallel and mixed highly deformed layers formed by minor faults, fractures, and sliding surfaces of variable orientations along with heterogeneous fault rocks. The fault core structure shows localized high strain zones mainly restricted to fault planes, with well-developed centimetric clay-rich gouges bounded by layers of clay-rich foliated rocks such as cataclasites (Fig. 4b), ultracataclasites (Fig. 4c), and fault breccias (Fig. 4d). The intense deformation that accommodates this area, obliterates the original structure and texture of the rocks precluding the protoliths recognition and generating anastomosed structural domains; however, elongated lenses (i.e. lithons) of ignimbrites (Fig. 4c) and clasts/blocks of granodiorites from basement rocks contained within an ultracataclasite matrix as well as volcanic clasts can be recognized. The coarse breccia shows cobble- to boulder-size clasts of ignimbrites (Fig. 4d). The damage zone - fault core transition is not exposed. Characterizing and discretizing the CF damage zone is complex due to the several superimposed COT fault segments and the protracted deformation since, at least, Ordovician. However, taking into account the main CF segment, the minimum damage zone is <0.3 km wide (Fig. 1c).

In situ permeability measurements across the CFZ span over a range of 4 orders of magnitude from 10^{-2} to 10^{1} D as shown in Fig. 4e. Permeability measurements in open fractures and in unconsolidated open-packed fault breccias show values that exceed the permeability measurement range (>10^2 D) and have not been considered. The fine-grained layers show mean permeability values that vary in a range from ~2 to 3 D, reaching 4 D in case of lithon, whereas fault gouge

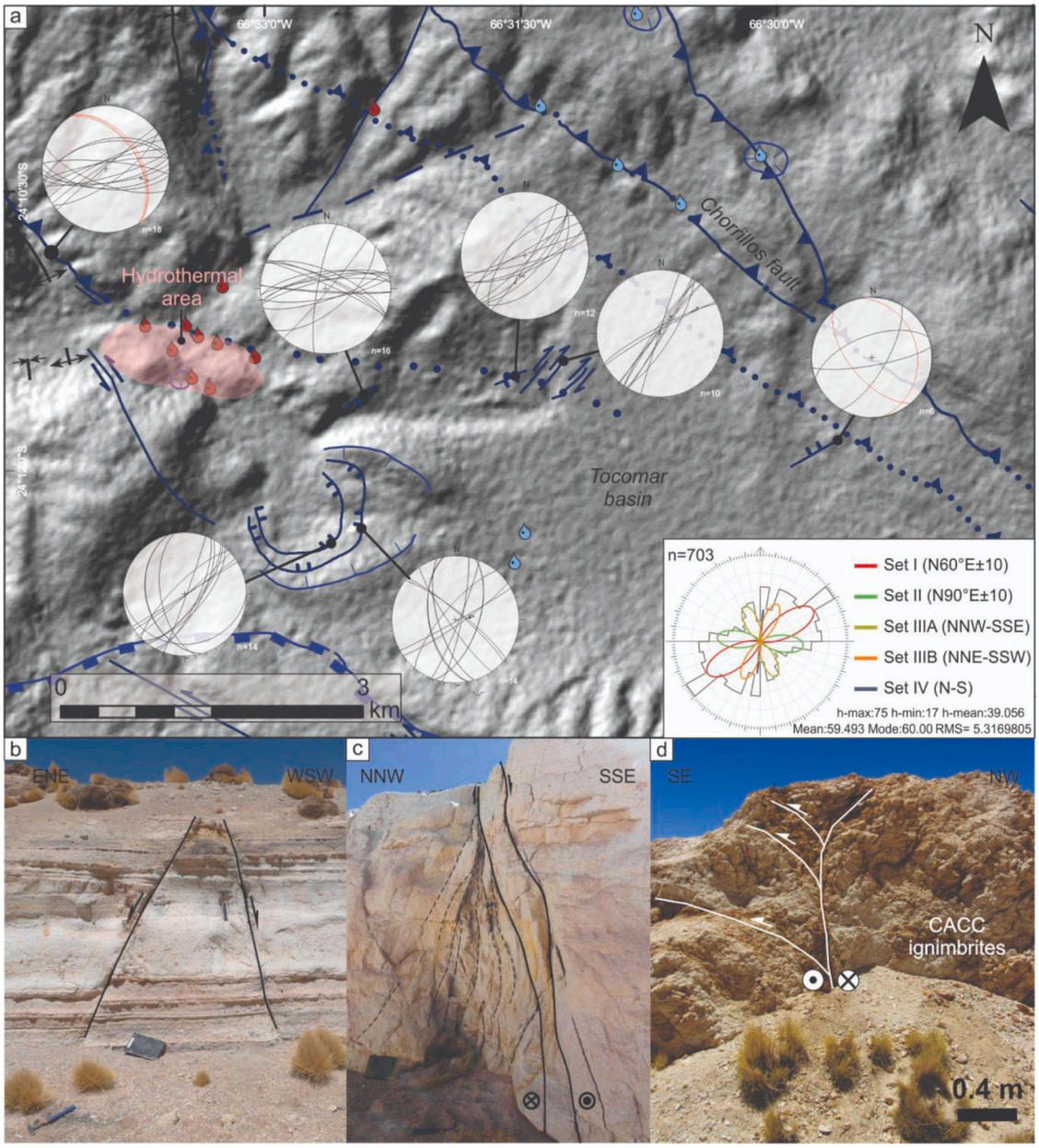

Fig. 3. (a) Shaded ALOS PALSAR DEM of the Tocomar area showing first- and second-order structures, and stereoplots of the surveyed structures. In the stereograms strike-slip and normal faults in black and reverse faults in red. All stereograms are lower-hemisphere, equal-area projection. In the inset, rose diagrams of azimuthal frequency of fractures. (b) Small-offset conjugate dip-slip normal fault affecting Quaternary deposits. c) Right-lateral strike-slip fault with normal component of motion developed within 0.55 Ma ignimbrites (Petrinovic et al., 1999) from the Alto Tocomar Formation. Riedel shears are indicated by dashed black lines. d) Positive flower structure within Cerro Aguas Calientes Caldera (CACC) ignimbrites controlled by left-lateral transpressive fault (For interpretation of the references to color in this figure legend, the reader is referred to the web version of this article).

shows consistently lower values that vary from 0.89 to 0.56 D (Fig. 4e). Conversely, the box plots (Fig. 4e) shows that the permeability drops sharply when measurements were made perpendicular to structural features, always being lower than 0.503 D to values of 0.06 D. Although the permeability of the damage zone could not be measured, damaged basement blocks in a gray cataclastic matrix show mean permeabilities of ~0.3 D (Fig 4e).

5.2. Tocomar hydrothermal features and alteration

According to the aims of this study, the lithostratigraphic units were grouped into two units to highlight the volcanic and geothermal activity: 1) pre-Tocomar basin units (PTU) including the Eastern Magmatic Belt, Geste Formation and CACC Ignimbrites, and 2) Quaternary Tocomar basin units (TBU). While the TBU show hydrothermal alteration, restricted to fractures and fault zones (Fig. 3c), it is assumed that due to the overall thickness (<200 m; Filipovich et al., 2020), they do not host the main geothermal reservoir. In the study area, the Eastern Magmatic Belt is intensely fractured and faulted. Spacing between joints ranges from 20 to 60 cm (Fig. 5a). Fractures often are filled by sediments and/or quartz crystals, but mostly they are open (Fig. 5a). In the Geste Formation the hydrothermal alteration consists of lithologically- and structurally-controlled discolored patches in conglomerates and sandstones (Fig. 5b), or alteration halos in fracture walls of mudstone (Fig. 5b). These deposits are also cut by hydrothermal breccia (i.e. breccia pipes) consisting of coarse cobble- to boulder-sized, subrounded to subangular fragments supported by a pebble-cobble iron-oxide matrix (Fig. 5c). The most pervasive alteration zones occur along an indurated

WNW-ESE ridge made by strongly altered CACC ignimbrites and fluvially reworked TBU deposits located at the intersection of orogen-parallel and COT-like faults (Fig. 3a). This alteration zone is characterized by a complex, closely spaced, fracture network with development of NE striking sub-vertical quartz-carbonate veins (Fig. 5d) and silicified hydrothermal breccia (Fig. 5e), that have the same strike of interbedded hydrothermal quartz (Fig. 5f). Furthermore, jigsaw and crackle breccias occur adjacent to crater rims (Fig. 5d).

In order to characterize the mineral assemblage several samples were collected across the altered ridge zone, as following: i) moderate to strong alteration (original textures obliterated), ii) weak to moderate alteration (strong bleaching), and iii) veins. Raman spectroscopic analysis suggests that K-feldspar and quartz±anatase (Fig. 5g, h) are present throughout the assemblage from the least to the most altered samples. There is a progression from central quartz and SiO_2 polymorphs in veins and silicified breccias (Fig. 5g), to alunite + jarosite/natrojarosite + K-feldspar ± gypsum zones (Fig. 5i), that grades into calcite + iron-oxides zones (Fig. 5j) in the outermost sectors.

5.3. Geochemical and isotopic composition of fluids

5.3.1. Chemical and stable isotopic ($\delta^{18}O$ and δ_D) composition of waters

The chemical-physical parameters as well as the chemical and isotopic composition of the studied waters are listed in Tables 1 and 2.

Thermal waters are Na-Cl(HCO_3) type, except TCM7 that shows a Na-HCO_3 composition (Fig. 6a, b and Fig. 7a). Thermal waters show slightly acidic pH values to near-neutral (5.84–6.87), and outlet temperatures and TDS values ranging from 30.3 to 70.2 °C, and from 1320 to 3151 mg/L, respectively. These waters are also characterized by relatively high concentrations of HCO_3^- (up to 827 mg/L), SiO_2 (up to 160 mg/L), B (up to 44 mg/L), Li^+ (up to 12 mg/L), Br^- (up to 0.69 mg/L), F^- (4.7 mg/L) and NH_4^+ (up to 6.5 mg/L). The Na^+ is the major cation showing concentrations of about one order of magnitude higher than those of the other cations (up to 952 mg/L) (Fig. 6a). As far as trace element concentrations is concerned (Table 2), the highest values were measured for As and Cs (up to 10,723 and 7406 μg/L, respectively), followed by Sr, Rb, Mn, Fe, Ba and Se (1468.4, 769.6, 605.9, 198.3, 138.5 and 4.12 μg/L, respectively). The oxygen and hydrogen isotopic data (expressed as $\delta^{18}O$-H_2O and δ_D-H_2O‰ vs. V-SMOW, respectively) vary in a narrow range, from -10.6 to -9.0 and from -84.2 to -80.9 ‰ vs. V-SMOW.

Based on the chemistry of the major ions, three types of cold waters can be distinguished (Figs. 6a and 7b): i) Ca-HCO_3 waters, representing the majority of the cold water samples, with low temperature and TDS values (≤22.1 °C and ≤674 mg/L, respectively) and acidic to slightly alkaline pH values (5.4–7.61); ii) Ca-Cl waters, represented by the creek (TZ1) located toward the NE of the Tocomar area, in the vicinity of the Tuzgle volcano (Fig. 2a), and having a slightly acidic pH (6.61), low temperature (10 °C) and TDS value of 889 mg/L; iii) Ca-SO_4 waters, i.e.

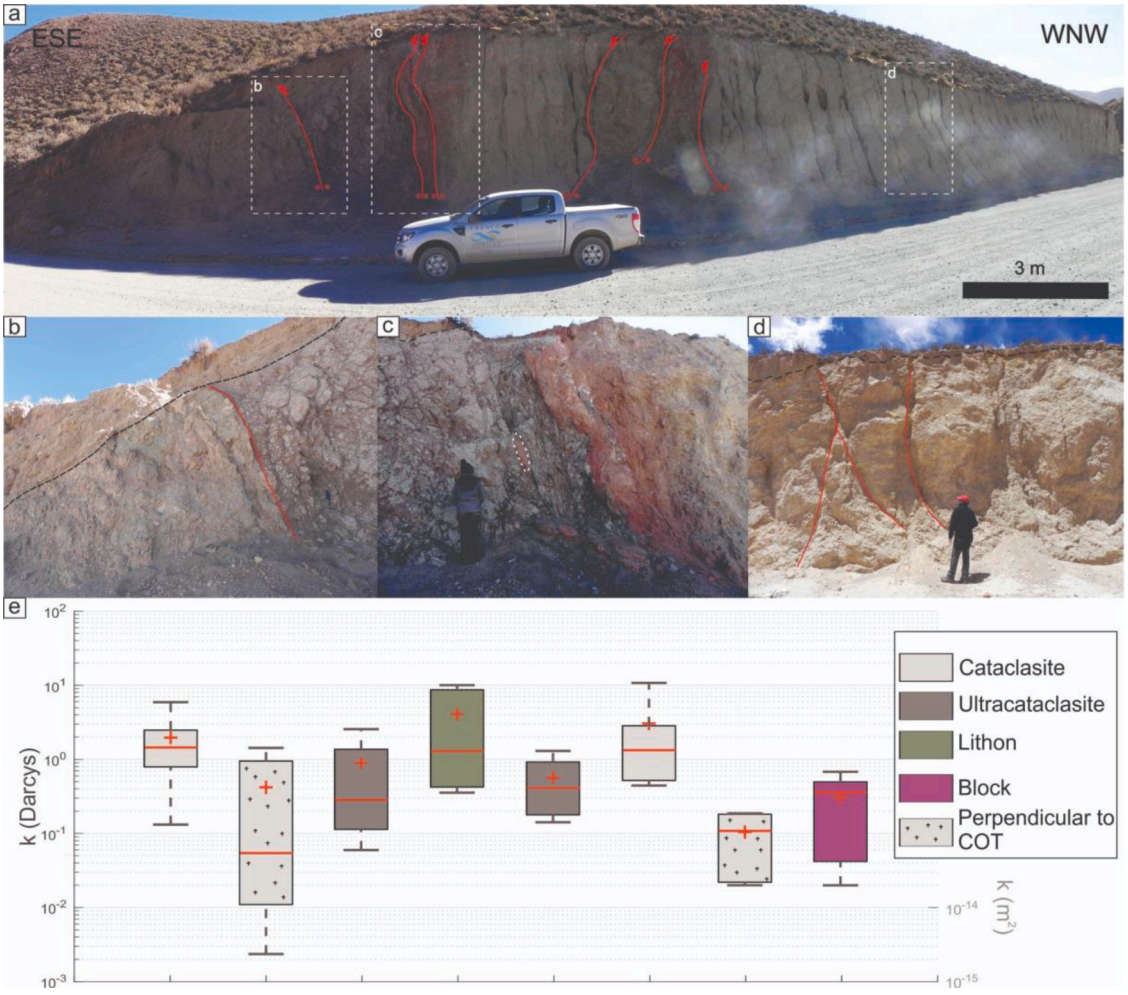

Fig. 4. (a) Field view of the Chorrillos fault zone and internal structure. Note the sub-parallel strands of fault cores. Insets indicate the location of detailed photos of fault core rocks. (b) Cataclasites (c) Ultracataclasites bounding lithon outlined in dashed white. Lihton is composed of CACC ignimbrites and elongated parallel to the main slip surfaces. Contact with Quaternary alluvium is shown with black dashed lines. (d) Incohesive mosaic breccia. (e) In-situ measured permeability data of fault-rock samples. When recognized, the protolith is indicated. Mean permeabilities are indicated by orange crosses. Error bars represent the relative error. Lithology references as in Fig. 1c (For interpretation of the references to color in this figure legend, the reader is referred to the web version of this article).

two cold water lagoons (FR1 and FR2) with near-neutral pH (6.96–7.24), temperature ≤7.9 °C, and relatively high TDS (up to 4153 mg/L) in the range that characterizes the thermal waters. The trace element concentrations in the cold waters are in general lower than thermal waters, with the only exception of Sr (up to 945.1 μg/L; Table 2). The isotopic composition (expressed as $\delta^{18}O$-H_2O and δ_D-H_2O ‰ vs. V-SMOW, respectively) vary in a wide range, from -10.0 to 2.5 and from -77.8 to -12.9 ‰ vs. V-SMOW.

5.3.2. Chemical and isotopic ($\delta\ ^{13}C$-CO_2, $\delta\ ^{13}C$-CH_4 and R/Ra) composition of gasses

The chemical and isotopic composition of the bubbling gasses of the TGS are shown in Table 3 (in mmol/mol).

Carbon dioxide is by far the most abundant dry gas compound (from 852 to 938 mmol/mol), followed by N_2 (up to 71.7 mmol/mol), H_2S (up to 5.2 mmol/mol), CH_4 (up to 3.55 mmol/mol), H_2 (0.025 mmol/mol) and He (0.0055 mmol/mol). Carbon monoxide was below the analytical detection limit (0.001 mmol/mol). Atmospheric gasses O_2, Ar and Ne are present in very low concentrations, up to 3.07, 1.73 and 0.0009 mmol/mol, respectively. Light hydrocarbons, whose total concentrations are up to 0.0076 mmol/mol, mainly consist of C_2-C_5 alkanes, ranging from 0.00005 mmol/mol (i-C_5H_{12}) to 0.0045 mmol/mol (C_2H_6). The $\delta^{13}C$-CO_2 values vary from -11.91 ‰ to -10.49 ‰ vs. V-PDB; whereas those of the $\delta^{13}C$-CH_4 from -37.2 to -36.2 ‰ vs. V-PDB. The Rc/Ra values (where Rc is the corrected isotopic ratio calculated according to the $^4He/^{20}Ne$ ratio) measured in two selected samples (TCM2 and TCM4) are 1.06 and 1.28, respectively.

5.4. Hydrogeological features

Three principal watersheds occur in the area: i) Tocomar-Antuco, ii) San Antonio de Los Cobres and iii) Tuzgle hydrological basins flowing toward the NW, the SE-NE, and the N, respectively (Fig. 8a). The hydrogeological surveys were carried out in the Tocomar hydrological sub-basin (Fig. 8b), considering Toc-A as a closing point. This sub-basin covers an area of about 109.2 km^2 and has a mean elevation of 4655 m. The main collector (Tocomar river) receives input from the Tocomar hot springs in its headwater and flows to NW towards a salar endorheic basin. This sub-basin is characterized by many ephemeral streams linked to sporadic storm events, mostly occurring from December to March (Fig. 8c); while the rest of the year has a marked water deficit (Sanci et al., 2020 and references therein). The existing cold springs are mainly associated with the NNW-SSE trending faults that crosscut the sub-basin (Figs. 3a and 8d).

The water flux measurements at the closing point Toc-A vary between 53 and 93.9 l/s, after the dry (November/14) and wet (April/15) season, respectively. However, this measurement point reflects the contribution from either the shallow local circuit (cold springs and streams) or the hot spring waters. In order to estimate the influence of the hydrothermal fluids into the Toc-A closing point and its seasonal variability, other fluxes recorded at different measurement points after the wet (Q_w) and dry (Q_d) season are analyzed in detail (Fig. 8b, c). In Fig. 8c, it can be seen that in the gaging points associated with streams that either not receive inputs from hydrothermal fluids upstream or the contribution is negligible (Toc-B, Toc-C and Toc-D), fluxes vary significantly, with Q_w/Q_d ratios >> 1, up to 4.5. Whilst, Toc-A gaging point (shallow local circuit plus hot spring water), is likely to reflect a more regular flow throughout the year (Q_w/Q_d ratio ~ 1.7). A rough approximation of the total flow rate of the hot springs can be calculated by subtracting the sum of Toc-B, Toc-C and Toc-D fluxes from the Toc-A flux, being ~24 and ~31 L/s for the wet and dry season, respectively. Accordingly, the hot springs probably have the most regular flow throughout the year, having Q_w/Q_d ratio ~ 0.7. The apparent increase in the hot spring flux in the dry season is interpreted as a greater influence of the hydrothermal-deep circuit into the Toc-A flux during this season.

6. Discussion

6.1. The role of structural elements in fluid circulation

The results of this study indicate that from El Oculto to the east, near the Chorrillos volcano (Fig. 1c), the COT is an intensely-deformed shear zone that is the result of the intersection and superposition of first- and second-order fault systems and fractures. Notably, in the Tocomar area, the interplay of fault bending, fault intersection, and displacement along oblique transfer zones not only generates the conditions for volcanic center emplacement (e.g., Petrinovic et al., 2006; Acocella et al., 2011; Norini et al., 2013), but also leads to favorable tectonic and structural settings for the location of geothermal systems (Faulds and Hinz, 2015; Jolie et al., 2021). These relationships are supported by structural field data. The bending of first-order structures from N-striking faults to NW-trending along the COT, causes the increase in fracture density localizing hydrothermal fluids. Hot springs and strongly altered rocks occur at the intersection of ~N-S and ~NW-SE fault systems, and spatially match with the highest lineament density areas (>9 km/km^2) observed by Giordano et al. (2013). On the other hand, the Tocomar basin deposits are cut by second-order faults and fractures preferentially oriented NNE-SSW to NE-SW that have been interpreted as Riedel shear structures related to the COT (Petrinovic and Colombo Piñol, 2006; Lanza et al., 2013; Norini et al 2013; Filipovich et al., 2020). For the western segment of the COT, three pulses of enhanced tectono-magmatic activity at 13–10 Ma, 8–6 Ma and <1.5 Ma have been proposed (Petrinovic et al., 2006). These tectonic-magmatic pulses may have promoted cycles of fluid pressure build-up, fluid overpressure, pressure drops and precipitation of hydrothermal minerals and healing (Cas et al., 2011). Thus, the episodic hydrothermal activity, in the Tocomar area, can be grouped in two main events: the first occurred in the Miocene, concomitant with the main magmatic event of the area, and was related to El Oculto high-sulphidation epithermal system (Gorustovich et al., 2011); the second took place in the Quaternary and was related to the <0.5 Ma TVC. The ongoing COT activity, since at least the Middle Pleistocene, likely promoted fractures opening and, to some extent, predictable patterns of new structural features that jointly enhance bulk permeability and the development of preferential conduits for fluid flow. The development of transient open fracture systems, along with the abovementioned crosscut relationship, enhanced vertical permeability and could have allowed rapid discharge of magmatic fluids, as well as of hydrothermal fluids, widespread mineralization and alteration, and eventually self-sealing. This process of pressure building and suddenly pressure drop can explain the development of pebble to cobble breccia pipes (Fig. 5c) and ubiquitous jigsaw-fit textures (Fig. 5d), both within PTU and TBU facies, through fluid-assisted brecciation (Cas et al., 2011). This cyclical behavior is also supported by the complex textures and structures within multi-banded carbonate and sinter veins (Fig. 5d, f) related to the crack-sealing mechanism (Ramsay, 1980). Crack-open period may have favored the efficient upwelling of deep hot fluids through NE-striking fractures and its surface precipitation forming sinter terraces and silicified breccia matrix. This precipitation process also occurred into the fractures filling with hydrothermal minerals sealing the near-surface system and starting again the build-up pressure process. These multiple crack-sealing events could have been active since at least <160 ka ruled by local tectonic stress and reactive fluids availability. While this structural control only explains the local widespread and abundant surficial evidence of hydrothermal activity, the mechanism of deep fluid migration and accumulation was likely controlled by first-order faults.

Fluid flow in the upper crust is strongly controlled by brittle deformation and the tectonic environment since permeability anisotropy depends on the orientation of the stress field (Rossetti et al., 2011; Faulkner and Armitage, 2013). In strike-slip fault zones, such as COT system, structural conduits for fluid flow develop in the σ_2 direction, parallel to the fault plane and orthogonal to the maximum horizontal

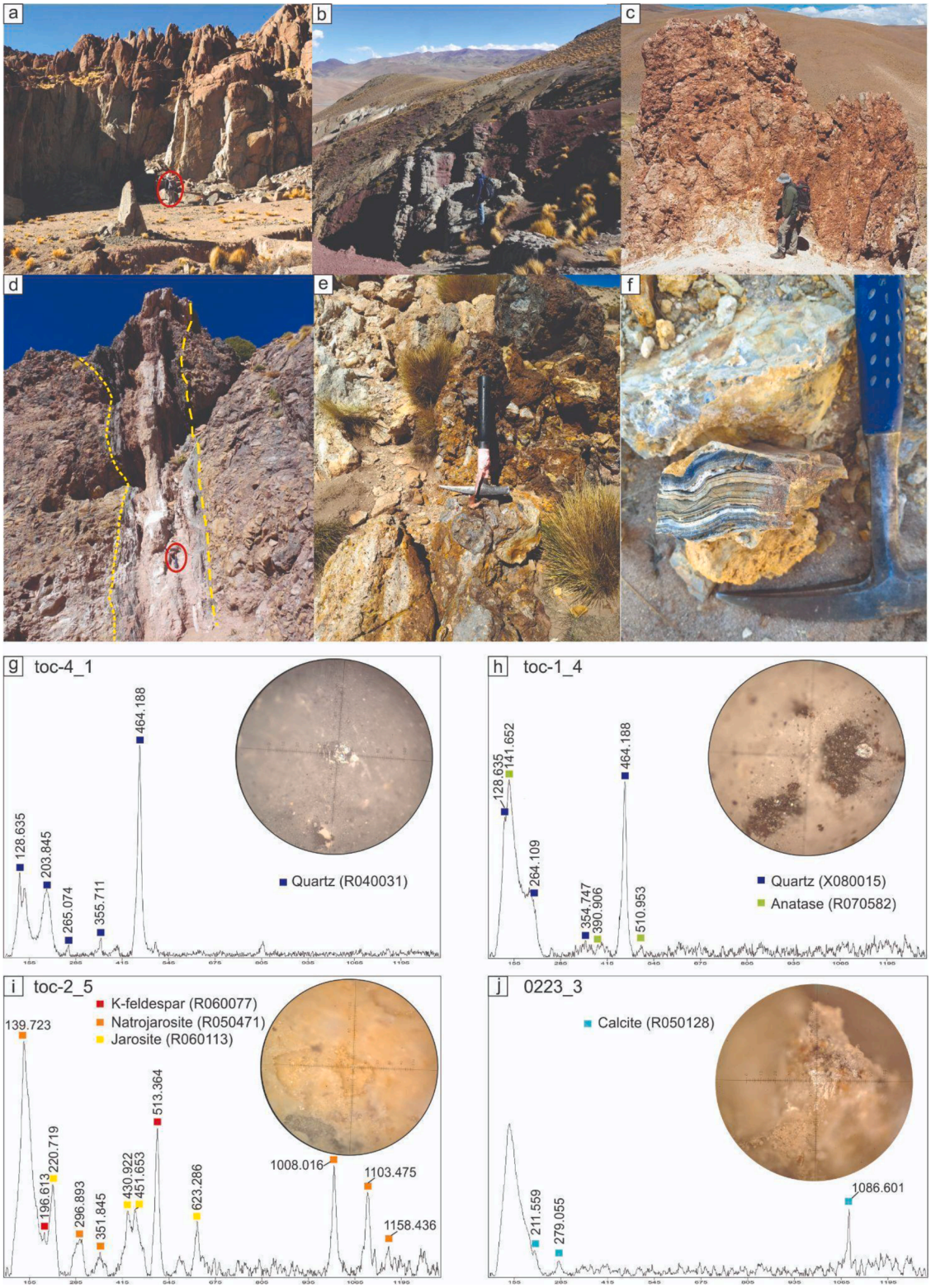

Fig. 5. (a) Ordovician basement rocks along Chorrillos high with parallel, unfilled, fractures. Person for scale (red circle). (b) Field view of breccia pipes within the Geste Formation. (c) Selective hydrothermal alteration controlled by facies variation. Note the abundant and widespread hydrothermal activity in coarse facies. (d) ~1 m wide carbonate vein cutting Miocene ignimbrites. Hammer for scale (red circle). (e) Silicified breccia within reworked Tocomar basin deposits. (f) Amorphous silica deposits with millimeter-scale banding. g), (h) Representative Raman spectra of most common mineral phases in strongly altered TBU deposits. i) Fine-grained mixture of K-feldspar, natrojarosite and jarosite. (j) Mixture of carbonate minerals (calcite±aragonite) in hydrothermal veins (For interpretation of the references to color in this figure legend, the reader is referred to the web version of this article).

Table 2
Chemical composition (in μg/L) of minor elements of cold and thermal waters from the Tocomar Geothermal System, Puna, Argentina.

ID	Mn	Fe	As	Se	Rb	Sr	Cs	Ba	Al
TCM4	47.04	198.32	1074.6	<1	769.6	1468.4	7406	138.54	45.98
TCM6	46.02	199	1069.4	4.12	768.4	1464.4	7174	135.46	50.94
TCM7	605.9	104.3	10,723	<1	400.1	227.7	2900	60.23	23.56
TOC2	116.5	139	29.58	<1	22.41	945.1	104.2	52.82	73.3
DR3	1.783	74.58	15.24	1.088	32.15	393.2	181.2	29.23	33.78

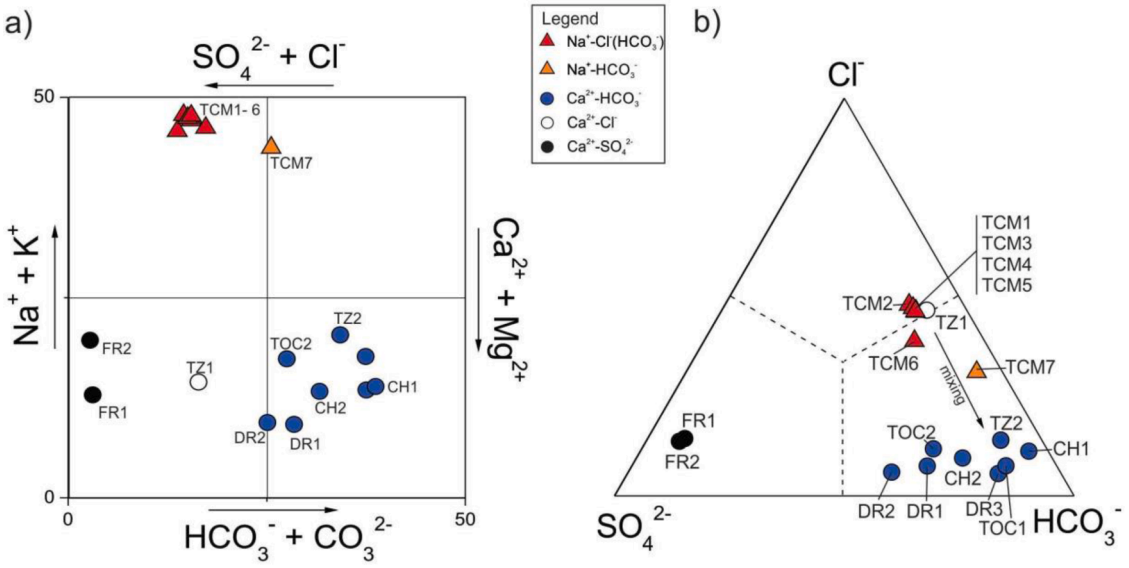

Fig. 6. (a) Langelier-Ludwing square diagram (Langelier and Ludwig, 1942) and (b) SO_4^{-2}- Cl^-- HCO_3^- ternary diagram for water samples from the TGS (in mg/L). Symbols are: red and orange triangles: thermal waters; blue, white and black circles: cold springs and stream water (for the interpretation of the references to color in this figure legend, the reader may refer to the web version of this article).

stress (Sibson, 1994, 1996). However, faults show different hydraulic behaviors acting either as i) effective barrier to cross-flow, ii) high permeability conduits or iii) combined conduit-barrier system (Caine et al., 1996; Bense et al., 2013). The preliminary analysis of the fault-zone structure suggests that in the studied area the CF (main segment of the COT) is a structurally heterogeneous multicore left-lateral transpressional fault with fault-perpendicular permeability variations (Fig. 4e). Across-fault permeability data are anisotropic, showing the highest permeability values parallel to the fault and fracture planes, drastically decreasing perpendicularly. These permeability variations could be related to deformation mechanism, episodic fault slip, lithology, and hydrothermal self-sealing (Sibson, 1994; Caine et al., 1996; Bense et al., 2013). In this sense, COT high-displacement faults, such as CF, can be classified as faults with preferential fault-parallel flux (i.e. focused flow) and as a barrier to cross-fault fluid flow (Caine et al., 1996; Rowland and Sibson, 2004). This behavior is highlighted by the alignment of the cold springs along the CF strike (Fig. 3a). Although in sandstones and loose sediments fault cores can reduce the permeability at least 4 orders of magnitude (Balsamo et al., 2010), faults affecting Quaternary deposits have vertical throw that never exceed ~1 m (i.e. 2nd order faults) and exhibit narrow fault zones restricted to the main fault surfaces (< 1 m). Hence, it can be inferred that the hydraulic conductivity is governed by the fault displacement and the core/damage zone ratio (e.g. Mitchell and Faulkner, 2012). In this context, first-order faults display complex fault zones with well-developed fault core or multicore with higher content of clay-sized material relative to simpler second-order faults that would not affect flow (Caine et al., 1996). However, as the COT is a multiple strands fault system (Norini et al., 2013), a more detailed analysis is required to constrain the factors that control fault-zone hydrogeology (e.g. Bense et al., 2013).

6.2. *Hydrogeochemical processes controlling the chemical and isotopic composition of fluids*

According to the δ^2H-H_2O vs. $\delta^{18}O$-H_2O binary diagram, where the Local Meteoric Water Line (LMWL: $\delta_D = (8.25 \pm 0.18)\ \delta 18O + (15.08 \pm 0.96)$‰; Dapeña and Panarello, 2011) was reported (Fig. 10a) the waters have a meteoric origin. The extreme climatic conditions of the Puna region characterized by large temperature variation, low humidity, strong winds, and scarce precipitations allow significant evaporation (Panarello et al., 1993), a process that produce kinetic fractionation (e.g. Fiorella et al., 2015; Bershaw et al., 2016), explaining the slight increase of both the δ^2H-H_2O vs. $\delta^{18}O$-H_2O values shown by the cold (surficial) waters. In agreement with this hypothesis, most cold waters plot along the theoretical evaporation lines (R1: $\delta^2H = 5.87\ \delta^{18}O - 14.50$ ‰ and R2: $\delta^2H = 5.66\ \delta^{18}O - 16.77$ ‰) constructed by Sanci et al. (2020) based on the particular climatic conditions of this area (Fig. 9). Thermal waters show a distinct distribution, suggesting the occurrence of a positive isotopic shift for $\delta^{18}O$ with minor δ^2H-enrichment, possibly due to water-rock isotopic exchange at relatively high temperature (> 150 °C; Truesdell and Hulston, 1980).

As shown in Fig. 7a, the chemical composition of the thermal waters (Na-Cl(HCO_3) type) suggests the occurrence of a deep hydrothermal aquifer, typically showing a Na-Cl composition, with relatively high HCO_3 contents possibly related to high amounts of CO_2, as suggested by the high $(HCO_3^- + CO_3^{2-})/(Ca^{2+})$ mol-ratios (up to 7.6). The relatively high TDS values (up to 3151 mg/L), slightly acidic pH and high concentrations of SiO_2, B, Cs, Li^+, Br^-, F^- and NH_4^+, i.e. common geochemical features of thermal springs in geothermal areas (e.g. Giggenbach, 1991; Aiuppa et al., 2006), support this hypothesis. The Na^+/Cl^- mol-ratios >1 indicate leaching of Na-silicates and alteration minerals (e.g. chlorite). Within all the hot springs, only the TCM7

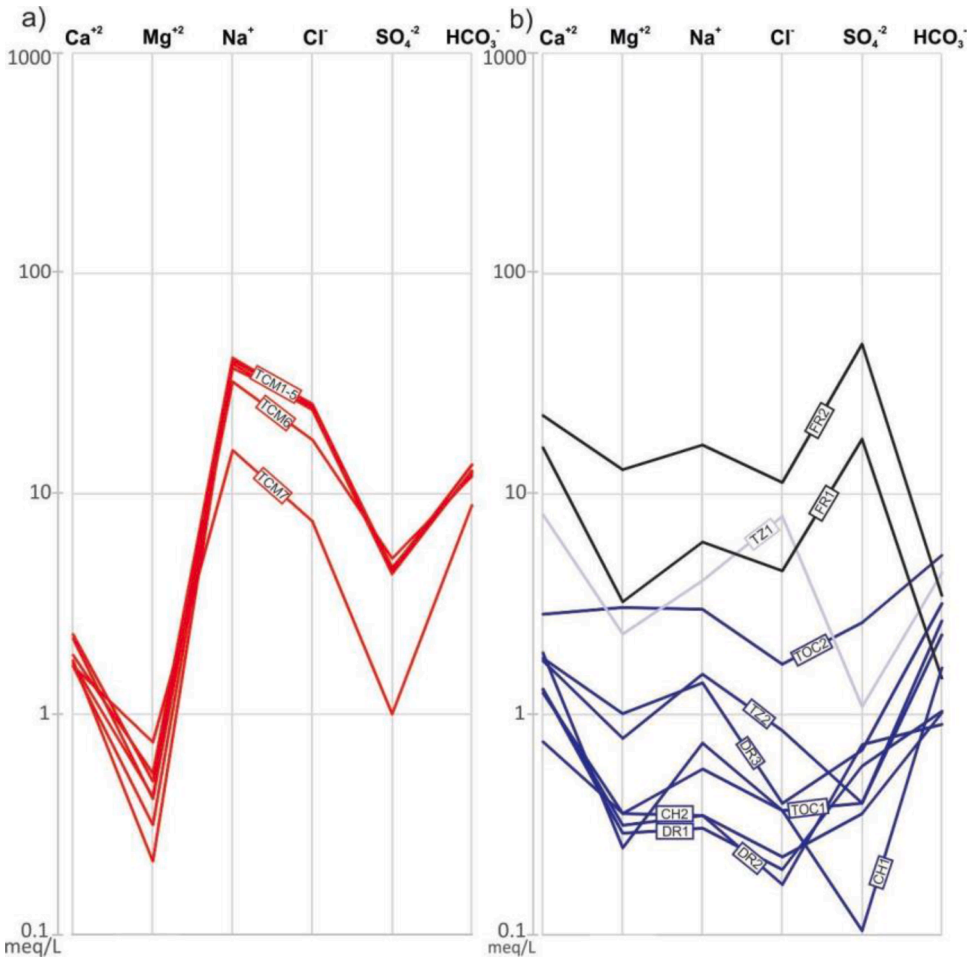

Fig. 7. Schoeller-Berkaloff diagrams for thermal (a) and cold (b) waters from the TGS.

sample appears to show signs of mixing with shallow dilute waters (like CH1 type; Figs. 6b and 7b), increasing its HCO_3^-, and Ca^{+2} and Mg^{+2} contents (Fig. 7a). The location of this sample, 2.7 km far from the rest of the hot springs that are clustered in a small area (~100 m^2; Fig. 2b) and directly above the CHF zone, can explain this chemical difference due to its distinct ascent pathway. The different circuits are shown in Fig. 16, Section 6.4. Among trace elements, it is noteworthy the high concentrations of As (up to 10,723 μg/L), in the range observed in some active geothermal fields (Webster and Nordstrom, 2003; Birkle et al., 2010), where has been attributed to high CO_2 concentrations in the source waters (Nordstrom et al., 2001). It is worth noting that this area is characterized by a high As- baseline into both geothermal and surficial waters (e.g. López et al., 2012; Hudson-Edwards and Archer, 2012; Sanci et al., 2020). In addition, local factors also play an important role in the control the high As-concentration of the TCM7 sample (10,723 μg/L) due to during the ascent pathway this thermal water interacts with the As-rich Cerro Aguas Calientes ignimbrites (Salado Paz et al., 2017), a process favoured by the pH value as well as the Na-bicarbonate composition of this sample (e.g. Nicolli et al., 1989, 2012; Alarcón-Herrera et al., 2013). The less reactive conservative components Li, Rb and Cs suggest the existence of secondary processes affecting even these relatively conservative alkali metals constituents (Section 6.4).

Cold waters having a Ca-HCO_3 composition (blue circles in Fig. 6a, b), represent surficial water (CH1 type hereafter) with the lower TDS values (≤674 mg/L; Fig.7b) and chemical composition similar to the meteoric rain water, evidencing their short circulation pathways. The Ca-SO_4 samples from the two cold water lagoons (FR1 and FR2), have the highest SO_4^{-2} contents (up to 2300 mg/L; Figs. 6b and 7b) and relatively high TDS (up to 4153 mg/L), comparable to those in the thermal waters. Interaction with gypsum seems to be the process that controls the sulfate content, being consistent with both the SO_4^{-2}/(Ca^{+2}+Mg^{+2}) mol-ratios ~ 1 as well as the saturation index (SI) <1 for gypsum phase, computed using the PHREEQC v. 3.2 (Parkhurst and Appelo, 1999) software package (llnl.database). These samples are also intensely evaporated (Fig. 9). Finally, the Ca-Cl type TZ1 sample from a creek located outside the Tocomar basin, into the vicinity of the Tuzgle volcano (Fig. 3), is likely due to mixing between a high-Cl end-member (likely representing a hydrothermal component, being in this case probably related to the Cl-Na hydrothermal reservoir of the Tuzgle geothermal system; Coira et al., 1995) and a shallow dilute HCO_3^- rich water (like CH1 type; Fig. 6b).

Regarding the gas phase of the TGS, the contribution from different sources can be analyzed in Figs. 10–12. The relatively low N_2/Ar ratios of the gas samples (Fig. 10a), in the range that characterizes air saturated waters (ASW; temperature dependent), exclude an extra-atmospheric source for N_2. Atmosphere-derived gasses recharging the hydrothermal aquifer are then the main source for N_2, Ar, and Ne. The low concentrations of these compounds suggest a strong gas contribution from an extra-atmospheric source (being the CO_2 the most abundant dry gas compound). The very low O_2/Ar ratios (up to 1.77) and relatively high H_2S contents, are typical features of hydrothermal reservoirs.

As respects to the origin of CH_4, the $\delta^{13}C$–CH_4 values (Table 3) suggest that CH_4 originated by thermocatalytic reactions of organic matter at hydrothermal conditions; however, the $CH_4/^3He$ ratios (Table 3) are close to the lower limit expected for typical thermogenic methane production (from 1×10^8 to 1×10^{12}; Poreda et al., 1988).

Table 3
Chemical composition (mmol/mol) of bubbling gasses from the Tocomar Geothermal System, Puna, Argentina. n.d.: not detected.

ID	CO_2	H_2S	N_2	CH_4	Ar	O_2	Ne	H_2	He	CO	C_2H_6	C_3H_8	i-C_4H_{10}	n-C_4H_{10}	i-C_4H_8	i-C_5H_{12}	n-C_5H_{12}	C_6H_6	$\delta^{13}C$-CO_2	Rc/Ra	He/Ne	$\delta^{13}C$-CH_4	$CH_4/^3He$
TCM1	895	5.2	51.9	0.98	1.25	1.44	0.0007	0.018	0.0028	n.d.	0.0032	0.00041	0.00011	0.00015	0.00033	0.00007	0.00009	0.0011	-10.62		4.00	-36.2	
TCM2	861	1.2	71.7	0.38	1.73	3.07	0.0008	0.011	0.0037	n.d.	0.0026	0.00035	0.00012	0.00013	0.00041	0.00006	0.00008	0.0015	-11.53	1.06	4.63		7.01E+07
TCM3	852	3.3	61	2.07	1.51	2.12	0.0008	0.019	0.0048	n.d.	0.0021	0.00026	0.00015	0.00011	0.00027	0.00008	0.00007	0.0009	-10.49		6.00	-37.2	
TCM4	876	4.1	46	2.06	1.12	0.88	0.0006	0.025	0.0055	n.d.	0.0033	0.00028	0.00017	0.00013	0.00031	0.00005	0.00006	0.0011	-10.65	1.28	9.17	-37.2	2.10E+08
TCM5	875	4.6	62.2	1.71	1.56	1.16	0.0009	0.023	0.0026	n.d.	0.0036	0.00041	0.00021	0.00014	0.00021	0.00007	0.00008	0.0012	-11.91		2.89		
TCM6	938	3.6	53	3.55	1.28	0.96	0.0007	0.015	0.0039	n.d.	0.0045	0.00046	0.00025	0.00018	0.00033	0.00011	0.00012	0.0016	-10.51		5.57		

According to the CH_4/C_{2+} vs. $\delta^{13}C$–CH_4 binary diagram (Fig. 11) proposed by Tassi et al. (2012), modified after Bernard et al. (1978), where C_{2+} is the sum of C_2–C_5 alkanes, hydrocarbons in the TGS are originated by thermogenic processes with CH_4 addition due to reduction of CO_2 and CO.

Fig. 10b shows that TGS samples fall in the field of volcano-hosted geothermal systems (Goff et al., 2000 and references therein), toward the highest CO_2 contents; with the exception of the TCM2 sample that falls near the CO_2 apex, which represents the range of travertine depositing springs and springs associated to fault systems (i.e. Crossey et al., 2009), being consistent with the geological context of the TGS.

According to the $CO_2/^3He$ ratios (up to 1.6×10^{11}; Fig. 12), which is two orders of magnitude higher than that of gasses released from the mantle, the origin of CO_2 is mainly related to a crustal source. The $\delta^{13}C$–CO_2 values measured in the bubbling gasses (Table 3) are slightly more negative than the mantle values (e.g. Rollinson, 1993; Sano and Marty, 1995; Ohmoto and Goldhaber, 1997), at a first approximation suggesting a significant biogenic CO_2 source. However, the occurrence of organic-rich sedimentary formations is unlikely considering the geological context of the TGS, which, on the contrary, would indicate thermometamorphic reactions involving limestones as the most reliable genetic process for this gas compound. Hence, the relatively low $\delta^{13}C$–CO_2 values of the TGS gasses are probably produced by isotope fractionation due to secondary processes, such as calcite precipitation, typically producing ^{13}C-depleted CO_2, and/or related to dissolution of gaseous CO_2 (Gilfillan et al., 2009; Barry et al., 2019).

The Rc/Ra values of the bubbling gasses up to 1.28, indicate a contribution of mantle-derived He up to 16% (considering a value of 8.01 as the most pristine mantle signature in the region; Robidoux et al., 2020), in the range of those found in other Andean geothermal systems of CVZ (from 0.92 to 5.52; e.g. Hilton et al., 1993; Hoke et al., 1994; Tassi et al., 2010; Peralta Arnold et al., 2017; Chiodi et al., 2019). This "low base level" of helium isotopes has been generally attributed to the abnormally thick crust existing in the Puna region (55–60 km; Yuan et al., 2000), where intra-crustal processes (mainly magma chamber degassing of the original mantle component and/or assimilation of ^4He-rich country rock), control the $^3He/^4He$ systematics (Hilton et al., 1993). However, it is important to highlight the role that petrogenesis could play in controlling helium isotopes, as it has been suggested for some magmatic geothermal systems in Southern Puna (Chiodi et al., 2019). In this sense, Petrinovic et al. (2006) proposed a strong crustal contribution for the magma genesis of the Tocomar volcanic center based on petrological studies ($^{87}Sr/^{86}Sr = 0.717$). Thus, the relatively low Rc/Ra values measured in the TGS gasses could additionally reflect this ^4He crustal input linked to the magma genesis.

6.3. Geothermometry

The equilibrium temperatures of the TGS hydrothermal reservoir were evaluated on the basis of the equilibrium reactions in the Na^+-K^+-Mg^{+2}-Ca^{2+} system (e.g. Giggenbach, 1991). As shown in the Na/400–K/10–$\sqrt{Mg}$ ternary diagram (Fig. 13a), TGS waters are in the field of partial equilibrium with the typical authigenic mineral assemblage at temperatures ranging from 223 to 235 °C. The only exception is represented by sample TCM7 that plots toward the Mg corner indicating a slightly lower temperature ~219 °C, probably caused by the mixing process suggested for this sample (Section 6.2). The ($10K^+$ / [$10\ K^+ + Na^+$] vs. $10Mg^{2+}$ / [$10Mg^{2+} + Ca^{2+}$]) geothermometer (Fig. 13b), which consider the effects of Ca^{2+} for the calculations into the mineral paragenesis (Chiodini et al., 1995), indicates equilibrium temperatures in agreement with those estimated by applying the Na/400–K/10–$\sqrt{Mg}$ geothermometer (Fig 13a).

Temperature estimations by applying the SiO_2 contents and Mg^{+2} ratios show lower temperature values than those calculated with the Na^+-K^+-Mg^{+2}-Ca^{2+} system (Table 4), likely due to secondary silica precipitation, a process that typically affects this geothermometer. In

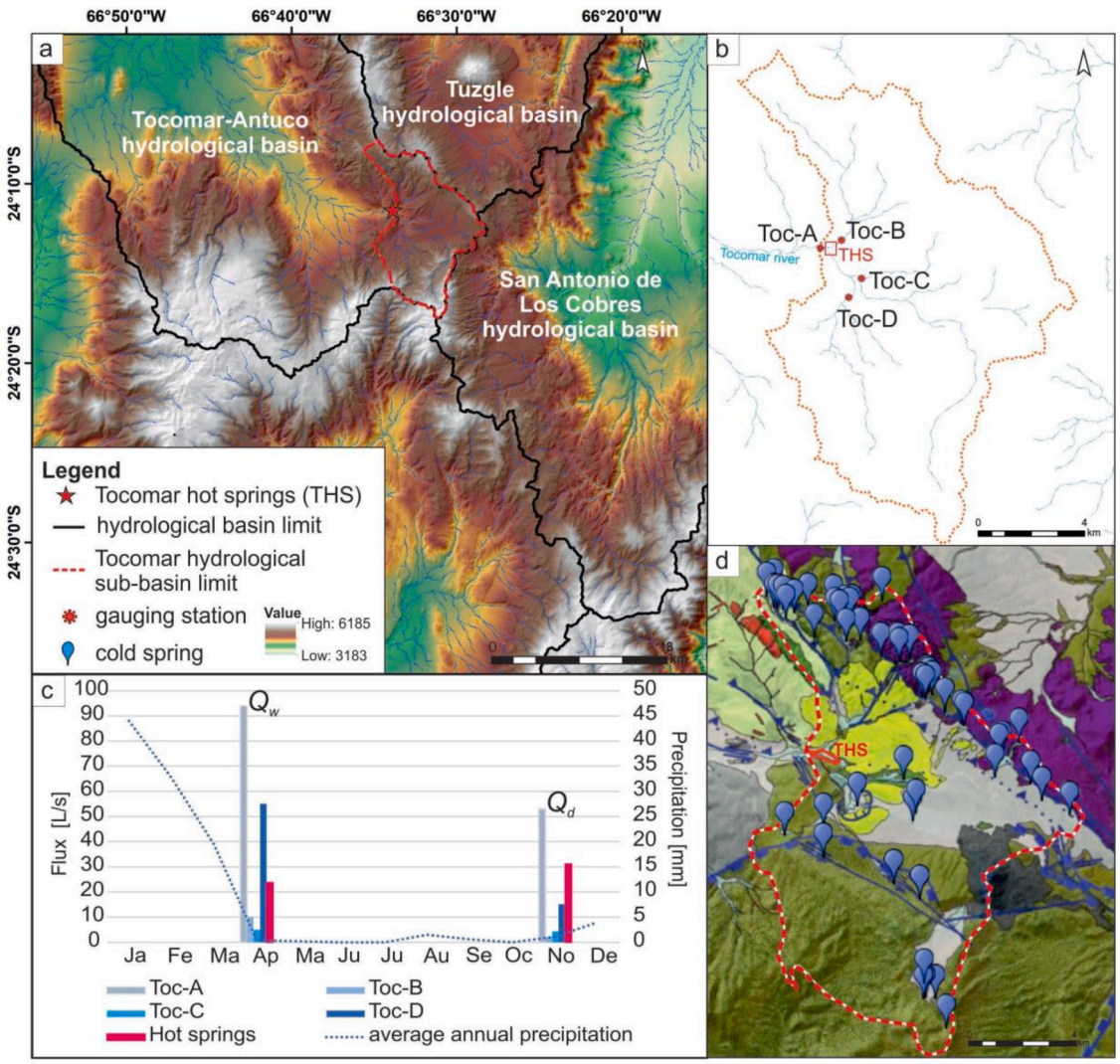

Fig. 8. (a) Main hydrological basins of the study area, (b) Detail of the Tocomar hydrological sub-basin showing the flow rate gaging stations. Red boundary: Tocomar hot spring area, c) Fluxes recorded at different measurement points after the wet (Q_w) and dry (Q_d) seasons. The estimated hot spring flux is also shown. Average annual precipitation from Bianchi et al. (2005), (d) Geological map of the Tocomar sub-basin showing the distribution of the cold springs related to the main tectonic structures. References as in Fig. 1c.

fact, the chalcedony geothermometer indicates temperatures ranging from 133 to 142 °C, which are similar to those computed with the K/$\sqrt{}$Mg geothermometer (from 95 to 145 °C), the latter being characterized by relatively fast kinetics and, consequently, strongly affected by re-equilibration during fluid uprising from the hydrothermal reservoir. Saturation index (SI = log AP/Ksp; where AP: ion activity product and Ksp: solubility product) for various mineralogical species from the outlet temperature 44.1 to 300 °C (using microcline to balance Al; Pang and Reed, 1998) was calculated with the PHREEQC v. 3.2 (Parkhurst and Appelo, 1999) software package (llnl: Lawrence Livermore National Laboratory database) for the sample that is closest to the full equilibrium line (TCM2; Fig. 13a, b). Minerals seem to achieve the equilibrium temperatures (considering an uncertainty of ±0.25) in the range from 151–176 °C (Fig. 14). These values are slightly higher than those previously calculated by the kinetically fast geothermometers in the liquid phase.

Fluid reservoir temperatures can be further investigated using gas compounds sensitive to changes of chemical-physical conditions. By combining the two temperature-sensitive species CO_2 and H_2 with the chemically inert constituent Ar, Giggenbach (1991) proposed the two CO_2/Ar and H_2/Ar geothermometers of Fig. 16a, assuming that Ar has a meteoric origin in hydrothermal reservoirs. Considering that hydrothermal fluids are O_2-free, to avoid the effect of possible air atmospheric contamination, Ar values were transformed into Ar*, as follows:

$$Ar^* = Ar - -O_2/22 \quad (2)$$

where the O_2/22 ratio is the minimum Ar concentration from air contamination. The dependence of H_2 on R_H in the two phases can be expressed, as follows:

$$\log(H_2/Ar*)_V = R_H + 6.52 - -\log(B_{Ar}) \quad (3)$$

$$\log(H_2/Ar^*)_L = R_H + 6.52 - \log(B_{H2}) \quad (4)$$

where B_{H2} and B_{Ar} are the vapor/liquid distribution coefficient of H_2 and Ar, respectively. At redox conditions controlled by the D'Amore and Panichi (1980) redox buffer (DP), the dependence of CO_2/Ar* ratios on temperature is given by:

$$\log(CO_2/Ar^*)_V = \log(PCO_2) - -5.51 + 2048/T + 6.52 - -\log(B_{Ar}) \quad (5)$$

$$\log(CO_2/Ar^*)_L = \log(PCO_2) - -5.51 + 2048/T + 6.52 - -\log(B_{CO2}) \quad (6)$$

where T is in K and B_{CO2} is the vapor/liquid distribution coefficient of

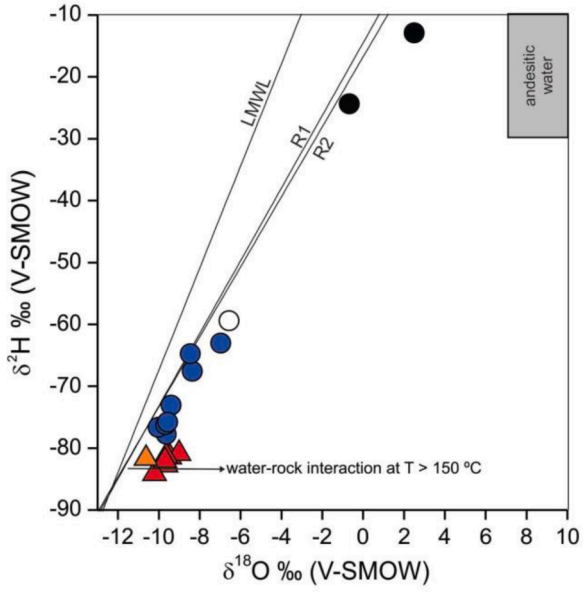

Fig. 9. δ^2H-H_2O vs. δ^{18}O–H_2O binary diagram for cold and thermal waters from the TGS. The Local Meteoric Water Line (LMWL: (δ_D = (8.25 ± 0.18) δ18O + (15.08 ± 0.96)‰; Dapeña and Panarello, 2011) is also shown. The TGS symbols as in Fig. 6.

CO_2 and the dependence of log(PCO_2) on temperature is given by:

$$\log(PCO_2) = 0.0168 \times t - -3.78 \quad (7)$$

where t is the temperature in Celsius degree.

Bubbling gasses of TGS are far from the equilibrium (Fig. 15a), possibly due to: (i) CO_2-H2 differential dissolution in a shallow aquifer, a process also considered to explain the CO_2 isotopic composition (Section 6.2), (ii) H_2 consumption by redox reactions occurring at relatively shallow depth where conditions are oxidizing, and/or (iii) Ar addition due to air contamination.

Chemical reactions involving CH_4 are kinetically slow, thus they can provide information about the equilibria attained at relatively high depth within the hydrothermal system (Giggenbach, 1991; Chiodini and Marini, 1998). Assuming that the CH_4-CO_2 pair is regulated by the Sabatier reaction ($CH_4 + 2H_2O \leftrightarrow CO_2 + 4H_2$) and that log fH2O = 4.9–1820 / T (Giggenbach, 1987), the dependence of the log(CO_2/CH_4) values on temperature and R_H in the vapor and the liquid phases can be expressed, as follows:

$$\log(CH_4/CO_2)_V = 4R_H + 5,181 / T(K) \quad (8)$$

$$\log(CH_4/CO_2)_L = 4R_H + 5,181 / T(K) + \log(B_{CO2}) - \log(B_{CH4}) \quad (9)$$

where B_{CO2} and B_{CH4} are the vapor/liquid distribution coefficients of CO_2 and CH_4, respectively. Eqs. (3), (4), (8) and (9) were used to construct the T–R_H grid in the CO_2–CH_4–H_2 system that is reported in the log(X_{H2}/X_{Ar*}) vs. log(X_{CH4}/X_{CO2}) diagram (Fig. 15b), assuming that the R_H values are controlled by the DP redox buffer system (D'Amore and Panichi, 1980). The TGS gasses seem to attain equilibrium temperatures with the fluid phase at lower temperatures (<150 °C) than those computed in the Na-K-Mg-Ca system (Fig. 13b). These apparent low equilibrium temperature values as well as the highly oxidizing conditions (RH < −3.6) are likely caused by H_2-consumption, as also suggested in Fig. 15a. Therefore, it is reliable to hypothesize that secondary

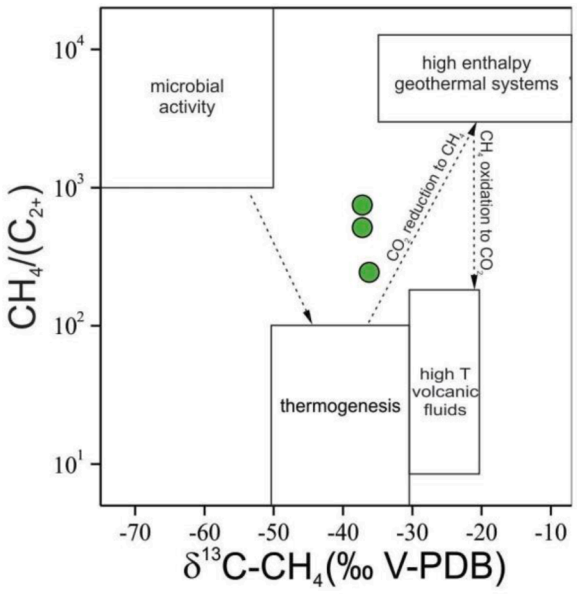

Fig. 11. δ^{13}C-CH_4 (‰ V-PDB) vs. $CH_4/(C_{2+})$ binary diagram for gasses from the TGS. Fields of microbial, thermogenic (Schoell, 1980, 1988; Whiticar 1999), and gasses from volcanic-hydrothermal systems (Tassi et al. 2012) are reported.

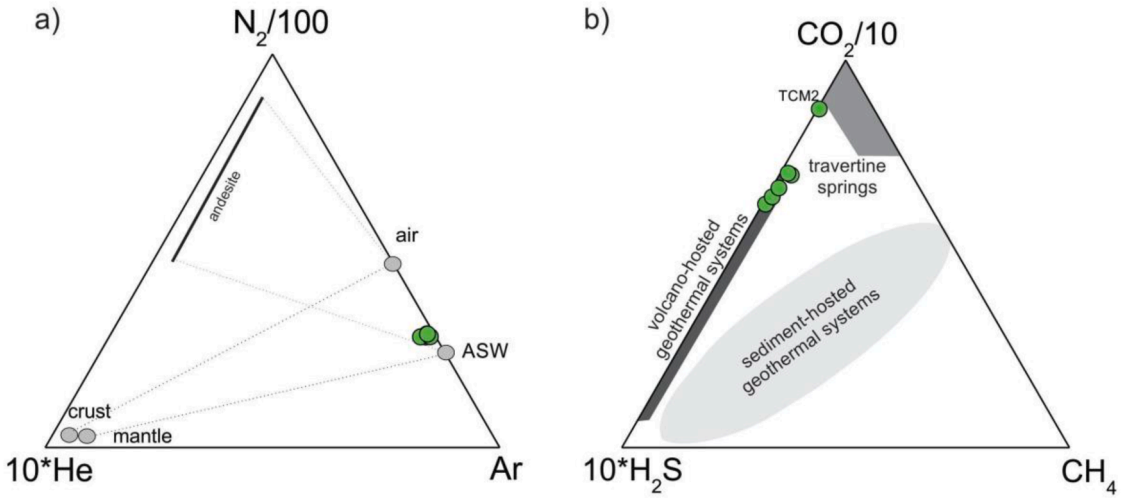

Fig. 10. (a) He–N_2-Ar ternary diagram and, (b) CH_4–CO_2–H_2S ternary diagram after Goff et al. (2000) for gasses from the TGS. Concentrations are in mmol/mol. The fields for volcano-hosted geothermal systems, sediment-hosted geothermal systems, and travertine spring gasses are also shown.

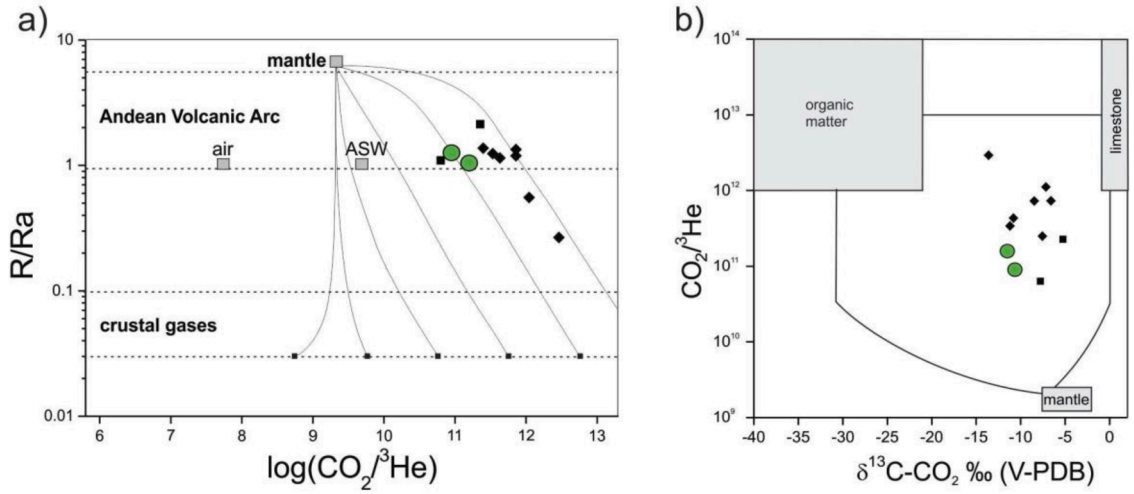

Fig. 12. (a) R/Ra vs. log($CO_2/^3He$) binary diagram for gasses from the TGS. Mixing curves between a mantle gas end-member and a crustal gas end-member with radiogenic helium and variable $CO_2/^3He$ ratios are shown. Between dashed lines, average values for Andean Volcanic Arc (Hoke et al., 1994) and crustal gasses (Hilton et al., 2002), (b) $CO_2/^3He$ vs. $\delta^{13}C–CO_2$‰ binary diagram for the gasses from the TGS. Isotopic values from others geothermal systems in the Puna plateau (Peralta Arnold et al., 2017; Chiodi et al., 2019) are shown for comparison. Symbols are: green circle: gasses from TGS; black diamond: data from Peralta Arnold et al. (2017); black square: data from Chiodi et al. (2019) (For interpretation of the references to color in this figure legend, the reader is referred to the web version of this article).

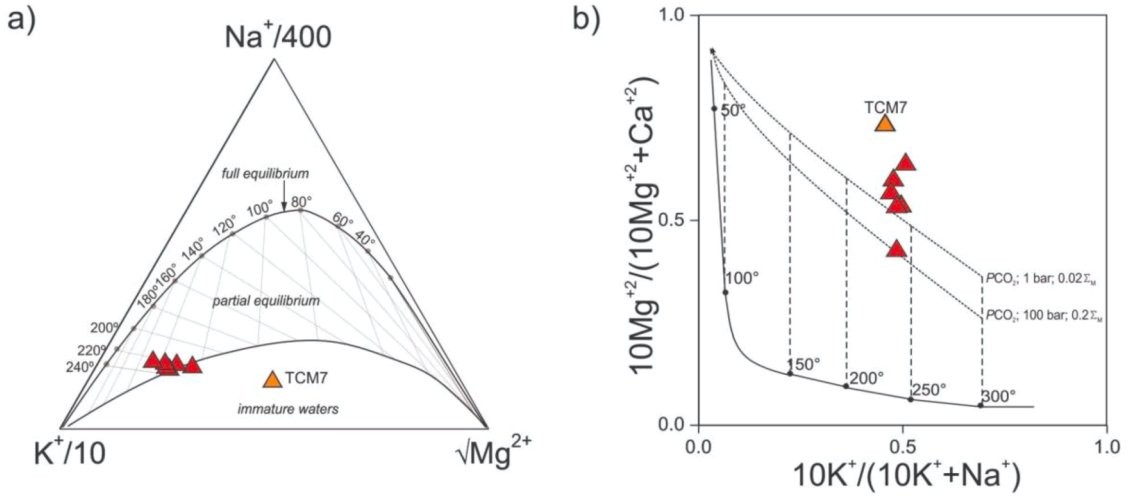

Fig. 13. (a) K^+-Na^+-Mg^{2+} ternary diagram (Giggenbach, 1988), for the thermal waters from TGS. The axes (Na/400-K/10-$\sqrt{Mg}$) were modified to enlarge the low temperature area of the diagram. Partial and full equilibrium curves from 40 to 240 °C are reported, (b) ($10K^+/[10K^+ + Na^+]$ vs. $10Mg^{2+}/[10Mg^{2+} + Ca^{2+}]$) binary diagram for the thermal waters from TGS. Equilibrium curves from 50 to 300 °C in presence of different mineral assemblages (Giggenbach, 1988; Chiodini et al., 1995) are reported.

Table 4
Equilibrium temperatures calculated for the thermal waters from the Tocomar Geothermal System, Puna, Argentina.

ID	T Na/K (Giggenbach, 1983)	T K^2/Mg (Giggenbach, 1986)	Quartz $_{no\ steam\ loss}$ (Fournier, 1973)	Quartz $_{with\ max.\ steam\ loss}$ (Fournier, 1973)	Chalcedony (Fournier, 1973)	α -Cristobalite (Fournier, 1973)	amorphous silica (Fournier, 1973)
TCM1	235	134					
TCM2	228	145	165	156	142	115	42
TCM3	231	136					
TCM4	225	131	157	150	133	107	35
TCM5	228	138					
TCM6	223	123					

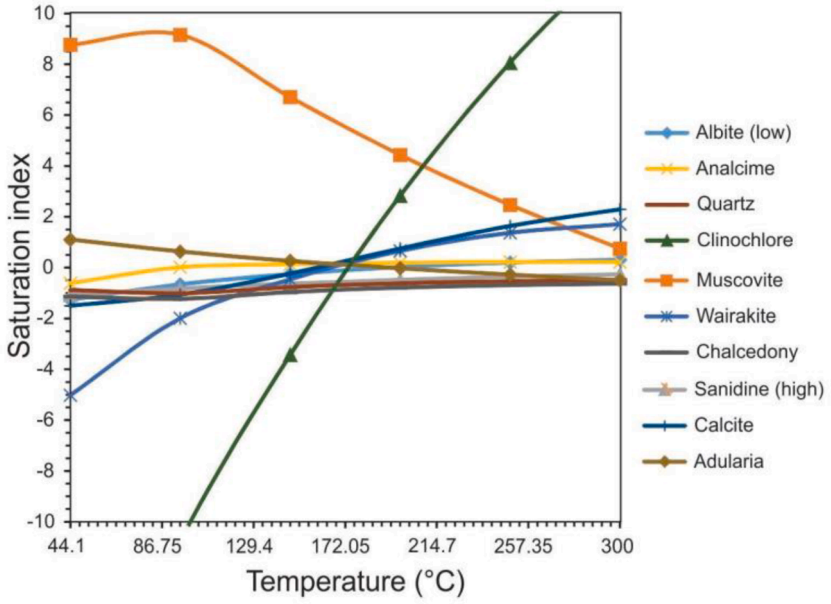

Fig. 14. Temperature (°C) estimated for the TCM2 thermal water from TGS by using the saturation indexes for various mineralogical species between the emergence temperature 44.1 and 300 °C.

processes are probably masking the chemical composition of the TGS gasses attained at depth.

6.4. Conceptual model of the Tocomar Geothermal System

Based on the integration of the results of this study along with petrophysical data (Gromoll, 2017) and MT data (Ahumada et al., 2017), a new conceptual model for the TGS is proposed (Fig. 16a,b). Ahumada et al. (2017) imaged with magnetotellurics an irregular subvertical COT-parallel low-resistivity feature (~10 Ω-m) with its shallowest top located towards Chorrillos high (Fig. 16a,b) at ~1–1.5 km depth. At this depth, the main reservoir could be hosted in the Ordovician basement rocks; however, it must be noted that the local plutonic undeformed basement rocks have low permeability (2×10^{-20}–1×10^{-19} m^2; Gromoll, 2017), compared to highly deformed zones where average permeability ranges from 8.9×10^{-13} to 3.05×10^{-12} m^2 (Fig. 4e). Since fault zones increase the permeability 7–8 orders of magnitude, permeable zones may be structurally linked to the COT (Fig. 4e). In this sense, the minimum permeability value for convective circulation of hydrothermal fluids is $> 1\times10^{-16}$ m^2 (Cathles et al., 1997), being around $>7\times10^{-13}$ m^2 in fault zones (López and Smith, 1995), which supports the idea that COT exerts a primary control on fluid pathways and accumulation. Furthermore, the COT is a seismically active fault zone (Schurr et al. 1999), providing localized and tectonically maintained vertical fluid pathways (e.g. Rowland and Sibson 2004). Nevertheless, there is still considerable ambiguity in defining COT width and its influence area spanning from 40 km (Chernicoff et al., 2002) to <10 km (Norini et al., 2013). Bonali et al. (2012) suggest that during Quaternary

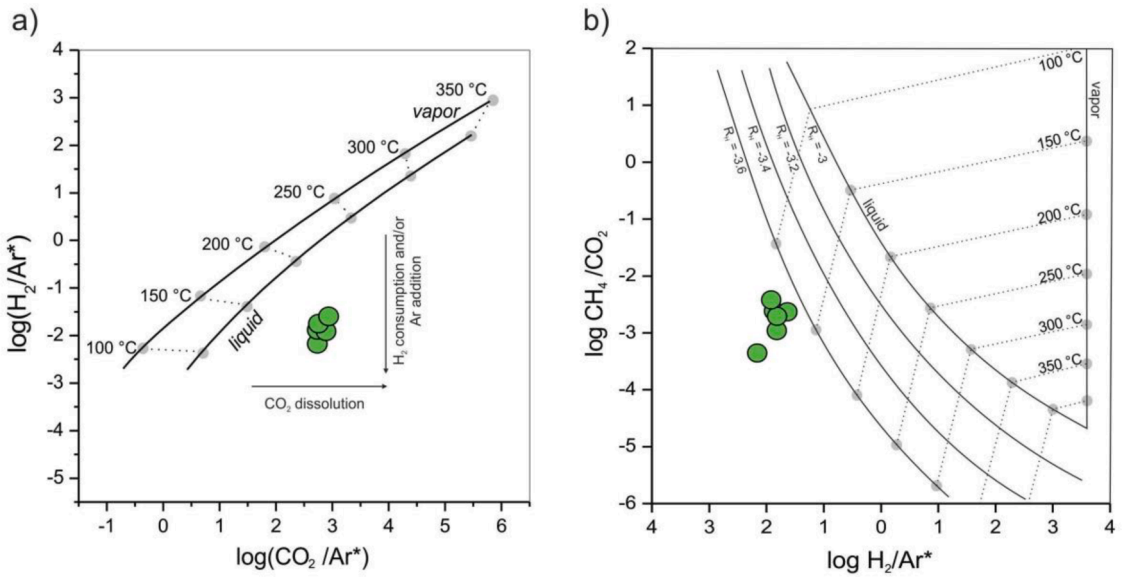

Fig. 15. (a) Log(H_2/*Ar) vs. log(CO_2/*Ar) binary diagram for gasses from the TGS. Solid lines refer to equilibria in the vapor and liquid phases controlled by the GT redox buffer system at temperatures from 150 to 350 °C (Giggenbach, 1987), (b) Log(H_2/*Ar) vs. log(CO_2/CH_4) binary diagram for gasses from TGS. Solid lines refer to equilibria in the vapor and liquid phases at temperatures from 150 to 350 °C and RH values from −3.0 to −3.6.

the most "active" sector of the COT is delimited by the Chorrillos seismogenic fault and subsidiary structures (Fig. 1c), pointing out its role in the reactivation of nearby structures. Consequently, based on the agreement between structural data, preliminary fault zone analysis, available geophysical and numerical data, permeability analysis and geochemical survey, the geothermal reservoir extent has been constrained to the CFZ (Fig. 16) and could be interpreted as a fault-controlled geothermal system. The conductive layers imaged by Ahumada et al. (2017) could be interpreted as a clay cap resulting of argillic alteration and self-sealing process (e.g. Facca and Tonani, 1967). The self-sealing process could deepen the high-temperature reservoir to depths >1000 m (e.g. Viggiano-Guerra and Gutiérrez-Negrín, 2005) capped by a low permeability layer that precludes vertical leaks. As opposed to reservoir rocks, cap rocks are usually formed by low tensile-strength rocks (Heap et al., 2020) and therefore they deform in a ductile manner. In this sense, based on the failure mode (i.e. brittle or ductile) the permeability within the reservoir appears to be maintained by the CF activity.

As shown in Fig. 16b, based on fluid chemistry and isotopy, two differentiated circuits are proposed, both of meteoric origin: i) a short surficial circuit, characterized by cold Ca(HCO_3-SO_4) waters and ii) a deeper hydrothermal circuit with Na-Cl(HCO_3) waters reaching temperatures up to 235 ºC. The possible paths of geothermal fluids can be inferred as follows (Fig. 16b): deep fluids could flow along the fault-fracture network related to the COT (i.e. feed zone) limited vertically by the low-porosity overburden made by basal units of the Geste Formation and altered CACC ignimbrites. Intersecting tectonic structures crosscut the cover layer promoting localized conduits that feed the TGS hot springs and could develop secondary reservoirs onto permeable facies of the Geste Formation by lateral flow (Giordano et al., 2013). The occurrence of the mineral facies cristobalite ± kaolinite ± alunite reflects the pH and temperature of the hydrothermal fluids (Elders and Moore, 2016). Despite the fact that the alteration in the Tocomar area could be related to the Miocene volcanic activity, it involves TBU;

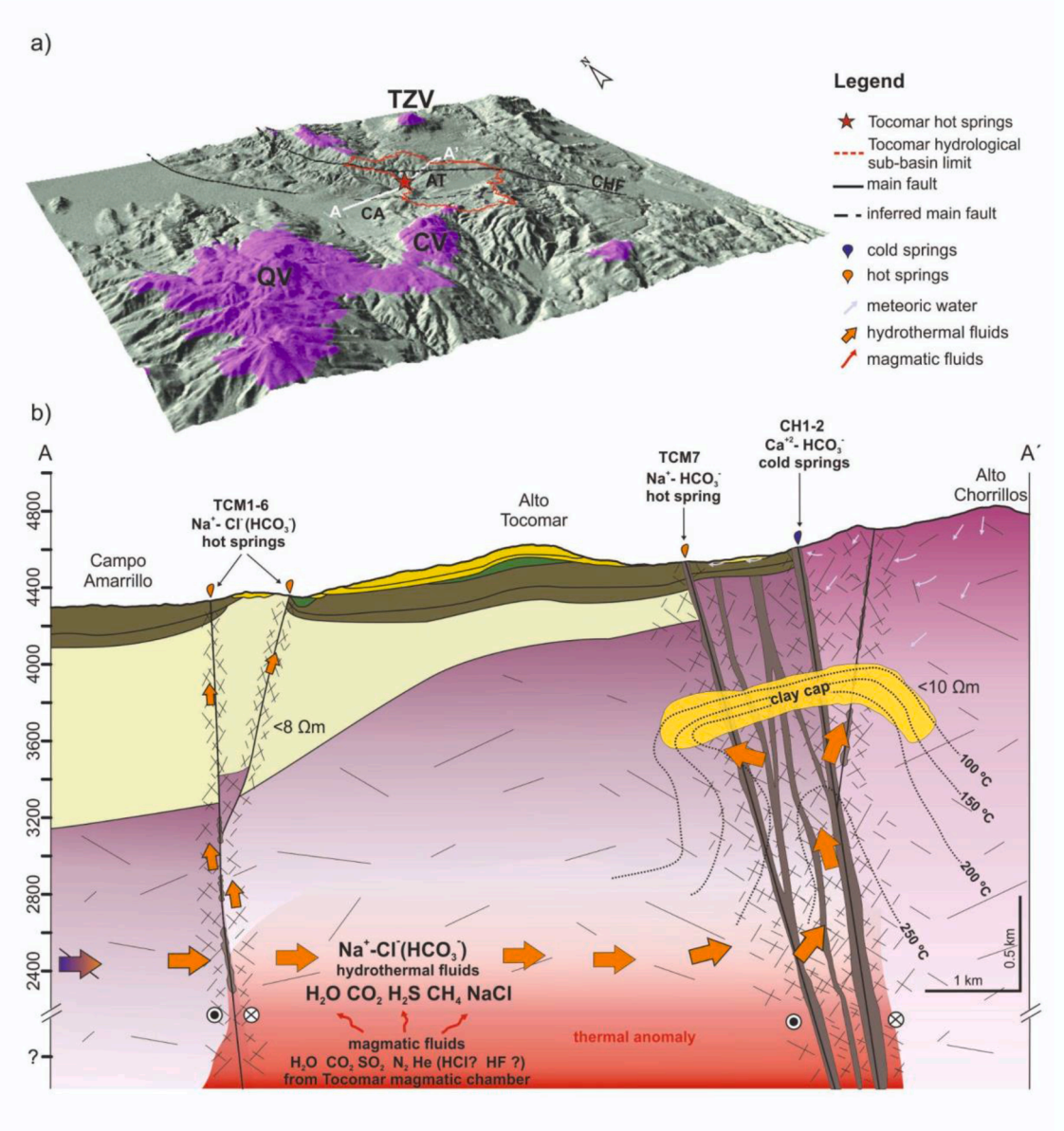

Fig. 16. (a) 3D-Hillshade DEM displaying areas with altitudes above 5000 m a.s.l. (purple areas). The schematic cross-section A-A' is also shown, (b) Conceptual model of the Tocomar Geothermal System in a schematic cross-section SW-NE oriented (A-A'). Resistivity values from Giordano et al. (2013) and Ahumada et al. (2017). TZV: Tuzgle volcano. QV: Quevar volcano. CV: Cerro Verde. CA: Campo Amarillo plain. AT: Alto Tocomar. CHF: Chorrillos fault. Lithology references as in *Fig. 1*c (For interpretation of the references to color in this figure legend, the reader is referred to the web version of this article).

therefore, it can be confidently interpreted to be related to the recent geothermal activity. Likewise, the strong vertical enhanced permeability in the multicore left-lateral transpressional CF is as high as to drive convection restricted to faults (i.e. focused flow), further enhanced by the magmatic heat, but limiting the lateral flow (Fig. 16b). This combined hydrological behavior supports the idea that the CF is the eastern boundary of the TGS, limiting fluid recharge from the east (Fig. 16a) and it is an independent hydrological system from the Tuzgle Geothermal System in contrast with previously proposed by Giordano et al. (2013).

The average infiltration altitude for the water recharging the main geothermal reservoir, calculated on the basis of water isotopes (δ^2H, $\delta^{18}O$; Table 1), is about 5300 m a.s.l. These results match those observed in earlier studies (>5000 m a.s.l.; Panarello et al., 1990) suggesting a scenario where the main geothermal reservoir likely has recharge areas outside the Tocomar hydrological sub-basin boundaries (purple areas are probable recharge zones in accordance with the isotope data in Fig. 16a). Although, to the south of Tocomar area the resurgent dome of the CACC reaches heights >5000 m a.s.l., the outcropping highly altered ignimbrites show permeabilities in the order of $x10^{-18}$ m^2 (Gromoll, 2017), reinforcing the hypothesis of a regional meteoric recharge probably toward the SW and W (Fig. 16a). Schurr et al. (1999), based on focal mechanisms, define a seismogenic zone at 7–8 km depth associated with the COT; therefore, it can be suggested that fluids can infiltrate and circulate preferentially along the subvertical oriented fracture mesh genetically associated with the COT at least to these depths (e.g. Rowland and Sibson, 2004). In addition, this long-term circulation pathway would favor the Li^+ enrichments shown by thermal waters, the high Na^+/Cl^- molar ratios (>1) and can explain the positive $\delta^{18}O$-shift (Fig. 9a), likely caused by prolonged water-rock interaction at temperature > 150 °C (Truesdell and Hulston, 1980). The low Rb contents are likely due to its uptake in illite; whereas, the low Li/Cs ratios are consistent with interaction processes with acidic rocks (Giggenbach, 1991) largely present in the area. Together these results provide first insights into the role of NW-striking structures on the TGS hydrothermal fluid discharges and reservoir formation. Further large-scale work would contribute to constrain the regional-scale structural control on fluid migration and emplacement of different geothermal systems (e.g. Veloso et al., 2020) spatially associated with the COT fault system (Fig. 2).

6.5. Preliminary resource assessment of the TGF

Different resource assessment methodologies based both on surficial, numerical, well, and production history data, with different levels of complexity and uncertainty to estimate the electric power potential are available (Ciriaco et al., 2020). Thus, the choice of method to use, and therefore the reliability and validity of the estimations, may depend on the available data and certainly on the project stage. Among all the resource assessment methods, the volumetric method combined with Monte Carlo simulations continues to be one of the most widely applied in the exploration stages (e.g. Williams et al., 2008a; Aravena et al., 2016; Barcelona et al., 2020). Since the original version (Nathenson, 1975; White and Williams, 1975; Muffler and Cataldi, 1978), the volumetric stored-heat method has undergone numerous updates and modifications (e.g. Williams et al., 2008b; Garg and Combs, 2010, 2015; Quinao and Zarrouk, 2014; Grant, 2018) mainly related to recovery factor, resource size and conversion efficiency aiming at reducing ambiguities and overestimations. However, being based on indirect measurements, this method has its limitations (e.g. Grant, 2014), and thus estimations must be analyzed with a probabilistic approach. Given the exploration stage of the Tocomar geothermal project, we used the method proposed by Garg and Combs (2015) for the reformulation of the volumetric method. This new method derives recoverable heat from specific power cycles (e.g. single-flash, binary), reducing ambiguities associated with reference temperature, by condenser temperature (T_c), and conversion efficiency (N_{conv}) (Eq. 10), while fluid properties are evaluated along the saturation line (Eq. 11) (Garg and Combs, 2015). Therefore, the electric power of a geothermal field for a single-flash power cycle is defined by the following equation:

$$We = \frac{W_{aflash} \times \eta_{conv}}{F \times L} \tag{10}$$

where F is the capacity or load factor, L is the plant life, and W_{Aflash} is the available work defined as:

$$W_{aflash} = \frac{\alpha(T_R - T_r)}{h_{sl}(T_r)}\{h_s(T_r) - h_l(T_r) - T_{cK}[s_s(T_r) - s_w(T_c)]\} \tag{11}$$

where $T_R$is the reservoir temperature, T_r is the reference temperature at separator conditions (5 bar, 151.831 °C), h_{sl}denotes the heat of vaporization at T_r, and $h$and s denote the enthalpy and entropy of liquid and steam phase (suffix l and s respectively). Here $\alpha$is defined as:

$$\alpha = R_f \times V \times \rho c \tag{12}$$

where R_f is the recovery factor, V is the reservoir volume, and ρc is the rock volumetric specific heat capacity.

Due to the uncertainty for determining reservoir volume (V) and temperature (T_R) as well as recovery factor (R_f) and load factor (F), a probability distribution function for the Monte Carlo simulation was assigned in order to generate a probabilistic forecast of potential capacity. Table 5 shows the values, ranges and assigned probabilistic distribution. In order to maintain a conservative effect in the calculations, biased distributions towards the minimum/conservative values were assigned (e.g. area, temperature).

The probable reservoir volume was estimated by Filipovich et al. (2017) based on magnetotelluric data from Ahumada et al. (2017). The minimum (5.20 km^2), most likely (6.20 km^2) and maximum probable resource area (9.74 km^2) were constrained by the resistivity contours of 10 Ω-m and 15 Ω-m that enclose the clay-cap units (~400 m thick) and constitute the upper thermal reservoir boundary. The reservoir thickness is a key parameter in Eq. (10) and again it is difficult to define precisely without drilling results (e.g. Grant, 2018); however, the thickness of the reservoir was estimated based on the depth of the resistivity layers of 10–60 Ω-m and 60–100 Ω-m minus the inferred depth at the clay-cap bottom within the anomaly zone beneath the dome-shaped conductive layer (<10 Ω-m) (Filipovich et al., 2017). Reservoir thickness is uniformly distributed ranging from 1000 m to 1400 m, in agreement with estimations for similar geothermal systems (Garg and Combs, 2010, 2015; Grant 2018), with minimum and maximum temperatures of 223 °C and 235 °C based on cation geothermometry (Table 4). Since the spatial distribution of permeability within the reservoir and the fraction of permeable volume are not constrained (e.g. Williams, 2014), we used a Rf uniformly distributed between 0 (not permeable horizon) and 0.20 as suggested by Garg and Combs (2015). The conversion efficiency (i.e. amount of energy that can be converted to electricity) for a liquid-dominated reservoir and single flash plant is calculated by $(0.0484 \times T_R - 0.5096) \times 0.01$(SKM, 2002). Then, considering a conservative reservoir temperature of 223 °C the calculated conversion efficiency is 10.3%, in agreement with available published data (Zarrouk and Moon, 2014; Ciriaco et al., 2020). Finally, the load factor was set from 80% to 95% (Ciriaco et al., 2020) following a uniform distribution (e.g. Barcelona et al., 2020).

Several electrical potential scenarios were generated, considering different probability distribution functions, ranks, and comparing with analogous geothermal systems in order to constrain the stochastic

Table 5
Input parameters values and distribution assigned for the Monte Carlo simulation. min.: minimum; m.l.: most likely; max.: maximum.

Input parameter	Symbol	Unit	Values			Distribution
			min.	m.l.	max.	
Area	A	km^2	5.25	6.2	9.74	Triangular
Thickness	Z	M	1000	-	1200	Uniform
Reservoir Temperature	T_R	°C	223	227	235	Triangular
Volumetric heat capacity	Pc	kJ $K^{-1}m^3$	-	2650	-	-
Recovery factor	R_f	%	0	-	20	Uniform
Separator temperature (5 bar)	T_r	°C	-	151.83		-
Condenser temperature	T_c	°C	-	40	-	-
Conversion efficiency	η_{conv}	%		10.3		-
Plant capacity factor	F	%	80.1	-	95	Uniform
Power plant life	L	Years	-	30	-	-

simulations. Also sensitivity tests were used to evaluate the degree of significance of the variables for each scenario. Fig 17a shows the results of the Monte Carlo Simulations by frequency histograms and the theoretical best-fit cumulative distribution function. Although several distributions were tested, the log-normal distribution provided a better fit under the AD (Anderson-Darling) hypothesis test. The performance curve (Fig. 17a) indicates that the probable electrical potential of the TGF for the P10, P50, and P90 cases are respectively 1.23, 6.18 and 11.67 MWe. The discrepancies with the previously calculated power output are related to the value of conversion efficiency. However, from the sensitivity analysis (Fig. 17b) we found that the recovery factor has a statistically significant effect in the simulation forecasts showing a strong linear correlation to the electric potential (Fig. 17c). These effects are mainly related to the uncertainty and limitations of the method to accurately predict reservoir permeability from complex, fracture dominated reservoirs (Williams, 2014). In this sense, since the input parameters are derived from surface data the estimated resources for the TGF must be classified as inferred resources and should be analyzed as such.

7. Conclusion and final remarks

The hydrogeochemical and structural investigations have shown that the TGF is a geothermal system independent from the Tuzgle geothermal system, with different hydraulic properties and conceptual models separated by an effective hydrogeological barrier made up by the Chorrillos fault. The COT fault system exerts first-order control on the development of the TGF by increasing the vertical permeability and providing the main pathways for ascent of hot, deep-seated fluids along NW-striking faults and the associated fracture mesh.

The TGF is a fault-controlled geothermal system hosted by, to a minimum extent, the CF at depths of 1000–1500 m below surface and lies within fractured Ordovician basement rocks. The main hydrothermal reservoir has a Na^+-$Cl^-$$(HCO3)^-$ composition with temperatures up to 235 °C sealed by a clay cap. The reservoir is mainly recharged by regional topography-driven groundwater flow and receives inputs of magmatic fluids from the degassing of the intra-crustal rhyolitic TVC magma chamber. The permeability values within the Chorrillos fault zone ($<9\times10^{-13}$ m^2) favor convective transport. Fluids upwelling along COT-related structural conduits and charging stratigraphic reservoirs in the Eocene Geste Formation cannot be completely ruled out.

The volumetric heat in place resource estimation method together with Monte Carlo simulations results predict a probable electric potential capacity above 1.23 MWe, 6.18 MWe, 11.67 MWe at the 90%, 50%, and 10% confidence level, respectively. The inferred resources are less than a third of the previously calculated power capacity (Filipovich et al., 2017). Given the scarce high-resolution geophysical data, a more stringent characterization of the resource size could improve the resource assessment. Finally, considering the magmatic fluid contribution, seismic activity, active faulting and local crosscutting patterns that imply higher bulk permeability; it could conceivably be hypothesised that the reservoir extent could be larger thus increasing the electric power potential. Furthermore, in many cases despite having excellent conditions in terms of heat anomalies and availability of fluids, the exploitation of geothermal resources in the Andes, is severely limited by logistic and technical aspects. This is not the case of the TGS since its strategic geographical location within the CPEH encourages to move forward towards more in-depth exploration phases. However, further work is required to assess the structural permeability and constrain the reservoir geometry in a 3D framework thus reducing risk and uncertainty in further stages.

CRediT authorship contribution statement

Rubén Filipovich: Conceptualization, Investigation, Formal analysis, Writing – original draft. **Agostina Chiodi:** Conceptualization, Methodology, Investigation, Writing – original draft. **Walter Báez:** Conceptualization, Writing – review & editing, Project administration. **Maria Florencia Ahumada:** Validation, Writing – review & editing. **Chiara Invernizzi:** Conceptualization, Writing – review & editing. **Sara Taviani:** Methodology, Resources. **Luca Aldega:** Writing – review & editing, Visualization. **Franco Tassi:** Resources, Writing – review & editing. **Alfonso Barrios:** Software, Data curation. **Sveva Corrado:** Resources, Supervision. **Gianluca Groppelli:** Writing – review & editing, Visualization, Supervision. **Gianluca Norini:** Writing – review & editing, Validation. **Sabina Bigi:** Validation, Supervision. **Chiara Caricchi:** Formal analysis. **Arnaldo De Benedetti:** Investigation. **Gianfilippo De Astis:** Investigation. **Raúl Becchio:** Investigation, Project administration. **José Germán Viramonte:** Supervision, Funding acquisition. **Guido Giordano:** Writing – review & editing, Project administration, Funding acquisition.

CRediT authorship contribution statement

Rubén Filipovich: Conceptualization, Investigation, Formal analysis, Writing – original draft. **Agostina Chiodi:** Conceptualization, Methodology, Investigation, Writing – original draft. **Walter Báez:** Conceptualization, Writing – review & editing, Project administration. **Maria Florencia Ahumada:** Validation, Writing – review & editing. **Chiara Invernizzi:** Conceptualization, Writing – review & editing. **Sara Taviani:** Methodology, Resources. **Luca Aldega:** Writing – review & editing, Visualization. **Franco Tassi:** Resources, Writing – review & editing. **Alfonso Barrios:** Software, Data curation. **Sveva Corrado:** Resources, Supervision. **Gianluca Groppelli:** Writing – review & editing, Visualization, Supervision. **Gianluca Norini:** Writing – review & editing, Validation. **Sabina Bigi:** Validation, Supervision. **Chiara Caricchi:** Formal analysis. **Arnaldo De Benedetti:** Investigation. **Gianfilippo De Astis:** Investigation. **Raúl Becchio:** Investigation, Project administration. **José Germán Viramonte:** Supervision, Funding acquisition. **Guido Giordano:** Writing – review & editing, Project administration, Funding acquisition.

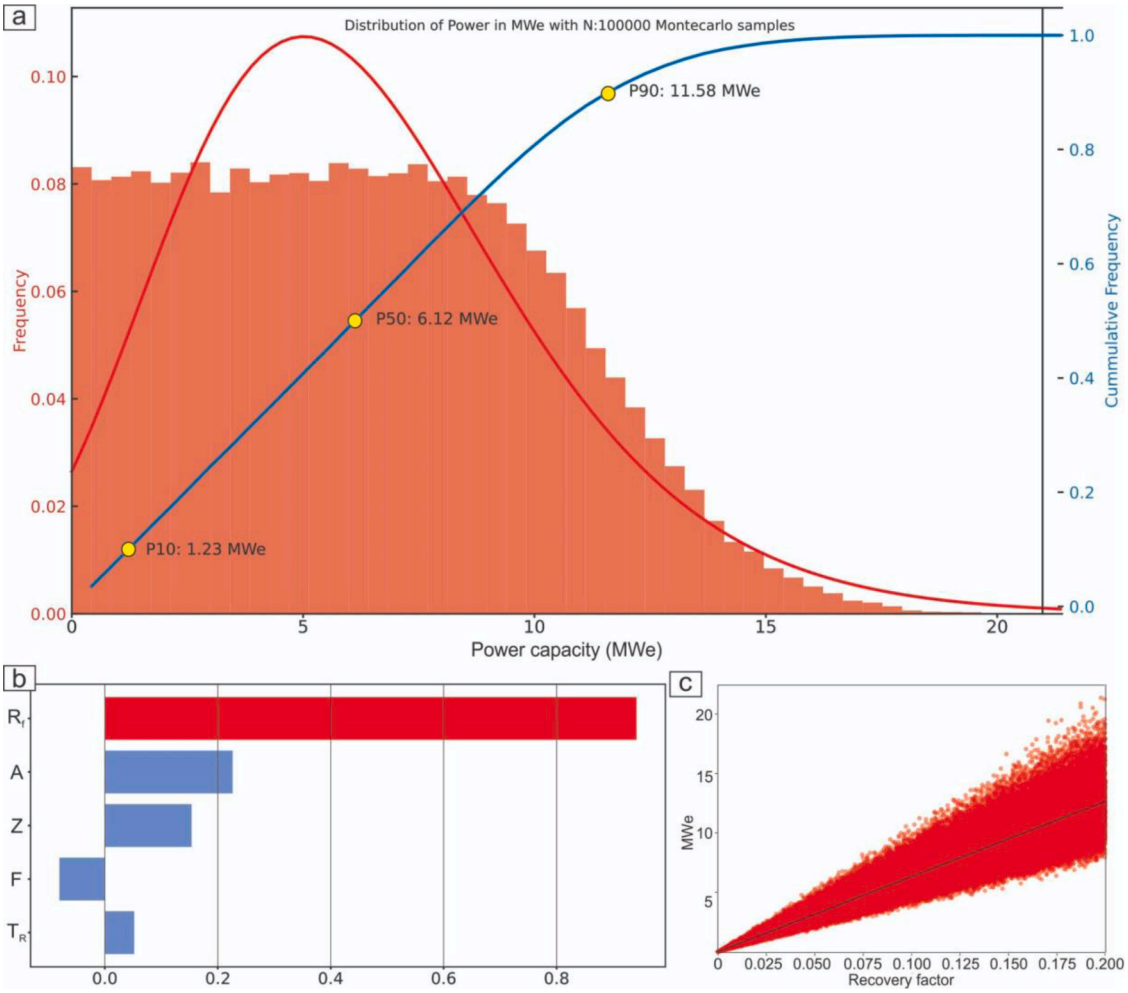

Fig. 17. Probabilistic resource estimation of the Tocomar Geothermal Field using volumetric method after 100,000 Monte Carlo iterations. a) Power capacity and best-fit empirical probability distribution function in red and empirical cumulative distribution function in blue. P10, P50 and P90 percentiles are shown. b) Sensitivity analysis for each model input. Symbols legend as in Table 5. c) Power potential as a function of recovery factor. Note the degree of correlation (For interpretation of the references to color in this figure legend, the reader is referred to the web version of this article).

Declaration of Competing Interest

The authors declare that they have no known competing financial interests or personal relationships that could have appeared to influence the work reported in this paper.

Acknowledgments

This work was supported by the Progetto di Grande Rilevanza MAE (Italy) MINCyT (Argentina) "Sviluppo sostenibile dei sistemi geotermici associati ai sistemi vulcanici della Puna nelle Province di Salta e Jujuy" (2014-2016; Resp. G. Giordano and J.G. Viramonte); PIO N° 3320140100015CO "Caracterización del Sistema Geotermal Tocomar y evaluación de su potencial como recurso energético no convencional sustentable para la Puna Argentina (YTEC; 2015-2017)". GN field work has been supported by Italgas project funds. The authors thank Donato Giovannelli and Shaunna Morrison for the Raman spectroscopic data. The contributions of Can Gromoll, Victor Borja Aramayo and Agustina Villagrán are also acknowledged. The authors also thank Dr. Rosa María Prol-Ledesma and an anonymous reviewer for their important contribution to the improvement of this manuscript.

References

Aceñolaza, F., Aceñolaza, G., 2005. La Formación Puncoviscana y unidades estratigráficas vinculadas en el Neoproterozoico-Cámbrico temprano del Noroeste Argentino. Latin Am. J. Sedimentol. Basin Anal. 12, 65–87.

Aceñolaza, F.G., Buatois, L.A., Mángano, M.G., Esteban, S.B., Tortello, M.F., Aceñolaza, G.F., 1999. Cámbrico y Ordovícico del noroeste argentino. Geología Argentina. Instituto de Geología y Recursos Minerales, Anales, pp. 169–187.

Acocella, V., Gioncada, A., Omarini, R., Riller, U., Mazzuoli, R., Vezzoli, L., 2011. Tectonomagmatic characteristics of the back-arc portion of the Calama-Olacapato-El Toro Fault Zone, Central Andes. Tectonics 30. https://doi.org/10.1029/2010TC002854.

Ahumada, M.F., Favetto, A., Filipovich, R.E., Chiodi, A., Báez, W., Viramonte, J.G., Guevara, L., 2017. Aplicación del método magnetotelúrico en la exploración del sistema geotermal Tocomar (Puna, NO Argentina). In: Grosse, P. (Ed.), XX Congreso Geológico Argentino. Asociación Geológica Argentina, Tucumán, pp. 3–8.

Aiuppa, A., Avino, R., Brusca, L., Caliro, S., Chiodini, G., D'Alessandro, W., Valenza, M., 2006. Mineral control of arsenic content in thermal waters from volcano-hosted hydrothermal systems: insights from island of Ischia and Phlegrean Fields (Campanian Volcanic Province, Italy). Chem. Geol. 229 (4), 313–330.

Alarcón-Herrera, M.T., Bundschuh, J., Nath, B., Nicolli, H.B., Gutierrez, M., Reyes-Gomez, V.M., Nuñez, D., Martín-Domínguez, I., Sracek, O., 2013. Co-occurrence of arsenic and fluoride in groundwater of semi-arid regions in Latin America: Genesis, mobility and remediation. J. Hazard. Mater. 262, 960–969. https://doi.org/10.1016/j.jhazmat.2012.08.005.

Allmendinger, R.W., Ramos, V.A., Jordan, T.E., Palma, M., Isacks, B.L., 1983. Paleogeography and Andean structural geometry, northwest Argentina. Tectonics 2, 1–16. https://doi.org/10.1029/TC002i001p00001.

Allmendinger, R.W., Jordan, T.E., Kay, S.M., Isacks, B.L., 1997. The evolution of the Altiplano-Puna Plateau of the Central Andes. Annu. Rev. Earth Planet. Sci. 25, 139–174. https://doi.org/10.1146/annurev.earth.25.1.139.

Alonso, R.N., 1992. Estratigrafía del Cenozoico de la cuenca de Pastos Grandes (Puna Salteña) con énfasis en la Formación. Rev. Asoc. Geol. Argentina 47, 189–199.
Aquater, A., 1979. Estudio Del Potencial Geotérmico De La Provincia de Jujuy, República Argentina. Secretaria de Estado de Minería. Contrato Saipen Argentina SA Gobierno de Jujuy.
Aquater, S.A., 1980. Exploración Geotérmica Del área del Cerro Tuzgle. Provincia de Jujuy, República Argentina. Secretaría de Estado de Minería, Open-File Report. Provincia de Jujuy, República Argentina.
Aravena, D., Muñoz, M., Morata, D., Lahsen, A., Parada, M.Á., Dobson, P., 2016. Assessment of high enthalpy geothermal resources and promising areas of Chile. Geothermics 59, 1–13. https://doi.org/10.1016/j.geothermics.2015.09.001.
Araya Vargas, J., Meqbel, N.M., Ritter, O., Brasse, H., Weckmann, U., Yáñez, G., Godoy, B., 2019. Fluid distribution in the central andes subduction zone imaged with magnetotellurics. J. Geophys. Res. 124, 4017–4034. https://doi.org/10.1029/2018JB016933.
Báez, W., De Astis, G., Filipovich, R.E., Giordano, G., Groppelli, G., Chiodi, A.L., Ahumada, M.F., Viramonte, J.G., Becchio, R.A., Norini, G., Taviani, S., De Benedetti, A.A., 2018. Variaciones relativas en la profundidad de la interacción agua-magma durante erupciones freatomagmáticas continentales. XVI Reunión Argentina de Sedimentología. Universidad Nacional de Río Negro, General Roca, p. 71.
Balsamo, F., Storti, F., Salvini, F., Silva, A.T., Lima, C.C., 2010. Structural and petrophysical evolution of extensional fault zones in low-porosity, poorly lithified sandstones of the Barreiras Formation, NE Brazil. J. Struct. Geol. 32, 1806–1826. https://doi.org/10.1016/j.jsg.2009.10.010.
Barcelona, H., Yagupsky, D.L., Wincour, D., Caselli, A., Cristallini, E.O., 2017. Modelo geológico estructural 3D del sistema geotérmico Copahue. In: Grosse, P. (Ed.), XX Congreso Geológico Argentino. Asociación Geológica Argentina, Tucumán, pp. 26–31.
Barcelona, H., Senger, M., Yagupsky, D., 2020. Resource assessment of the Copahue geothermal field. Geothermics 101987. https://doi.org/10.1016/j.geothermics.2020.101987.
Barnes, J.B., Ehlers, T.A., 2009. End member models for Andean Plateau uplift. Earth Sci. Rev. 97, 105–132. https://doi.org/10.1016/j.earscirev.2009.08.003.
Barry, P.H., de Moor, J.M., Giovannelli, D., Schrenk, M., Hummer, D.R., Lopez, T., Pratt, C., Alpízar Segura, Y., Battaglia, A., Beaudry, P., Bini, G., Cascante, M., d'Errico, G., di Carlo, M., Fattorini, D., Fullerton, K., Gazel, E., González, G., Halldórsson, S., Iacovino, K., Kulongoski, J., Manini, E., Martínez Miller, H., Nakagawa, M., Ono, S., Patwardhan, S., Ramírez, C., Regoli, F., Smedile, F., Turner, S., Vetriani, C., Yucel, M., Ballentine, C., Fischer, T., Hilton, D., Lloyd, K., 2019. Forearc carbon sink reduces long-term volatile recycling into the mantle. Nature 568 (7753), 487.
Bencini, A., 1985. Applicabilità del metodo dell'Azometina-H alla determinazione del boro nelle acque naturali. Rendiconti Societa Italiana di Mineralogia e Petrologia 40, 311–316.
Bense, V.F., Gleeson, T., Loveless, S.E., Bour, O., Scibek, J., 2013. Fault zone hydrogeology. Earth Sci. Rev. 127, 171–192. https://doi.org/10.1016/j.earscirev.2013.09.008.
Bernard, B.B., Brooks, J.M., Sackett, W.M., 1978. Light hydrocarbons in recent Texas continental shelf and slope sediments. J. Geophys. Res. 83, 4053–4061.
Bershaw, J., Saylor, J.E., Garzione, C.N., Leier, A., Sundell, K.E., 2016. Stable isotope variations (δ18O and δ_D) in modern waters across the Andean Plateau. Geochim. Cosmochim. Acta 194, 310–324.
Bianchi, A.R., Yañez, C.E., Acuña, L.R., 2005. Base de Datos Mensuales de Precipitaciones del Noroeste Argentino 41.
Blasco, G., Zappettini, E.O., Hongn, F., 1996. Hoja Geológica 2566-I, San Antonio De Los Cobres, Boletin 21. ed. Programa Nacional de Cartas Geológicas de la República Argentina.
Bona, P., Coviello, M., 2016. Valoración y Gobernanza De Los Proyectos Geotérmicos En América del Sur. Comisión Económica para América Latina y el Caribe (CEPAL.
Bonali, F.L., Corazzato, C., Tibaldi, A., 2012. Elastic stress interaction between faulting and volcanism in the Olacapato-San Antonio de Los Cobres area (Puna plateau, Argentina). Global Planet. Change 90–91, 104–120. https://doi.org/10.1016/j.gloplacha.2011.08.002.
Caine, J.S., Evans, J.P., Forster, C.B., 1996. Fault zone architecture and permeability structure. Geology 24, 1025–1028.
Carrapa, B., DeCelles, P.G., 2008. Eocene exhumation and basin development in the Puna of northwestern Argentina. Tectonics 27. https://doi.org/10.1029/2007TC002127.
Cas, R., Giordano, G., Balsamo, F., Esposito, A., Lo Mastro, S., 2011. Hydrothermal breccia textures and processes: Lisca bianca islet, panarea volcano, Aeolian Islands, Italy. Econ. Geol. 106, 437–450. https://doi.org/10.2113/econgeo.106.3.437.
Cathles, L.M., Erendi, A.H.J., Barrie, T., 1997. How long can a hydrothermal system Be sustained by a single intrusive event? Econ. Geol. 92, 766–771. https://doi.org/10.2113/gsecongeo.92.7-8.766.
Chernicoff, C.J., Richards, J.P., Zappettini, E.O., 2002. Crustal lineament control on magmatism and mineralization in northwestern Argentina: Geological, geophysical, and remote sensing evidence. Ore Geol. Rev. 21, 127–155. https://doi.org/10.1016/S0169-1368(02)00087-2.
Chiodi, A., Tassi, F., Báez, W., Filipovich, R., Bustos, E., Glok Galli, M., Suzaño, N., Ahumada, M.F., Viramonte, J.G., Giordano, G., Pecoraino, G., Vaselli, O., 2019. Preliminary conceptual model of the Cerro Blanco caldera-hosted geothermal system (Southern Puna, Argentina): Inferences from geochemical investigations. J. South Amer. Earth Sci. 94, 102213 https://doi.org/10.1016/j.jsames.2019.102213.
Chiodini, G., Marini, L., 1998. Hydrothermal gas equilibria: the H2O-H2-CO2-CO-CH4 system. Geochim. Cosmochim. Acta 62 (15), 2673–2687.
Chiodini, G., Frondini, F., Marini, L., 1995. Theoretical geothermometers and PCO2 indicators for aqueous solutions coming from hydrothermal systems of medium-low temperature hosted in carbonate-evaporite rocks. Application to the thermal springs of the Etruscan Swell, Italy. Appl. Geochem. 10 (3), 337–346.
Ciriaco, A.E., Zarrouk, S.J., Zakeri, G., 2020. Geothermal resource and reserve assessment methodology: overview, analysis and future directions. Renew. Sustain. Energy Rev. 119, 109515 https://doi.org/10.1016/j.rser.2019.109515.
Cladouhos, T.T., Allmendinger, R.W., Coira, B., Farrar, E., 1994. Late cenozoic deformation in the Central Andes: fault kinematics from the northern Puna, northwestern Argentina and southwestern Bolivia. J. South Amer. Earth Sci. 7, 209–228. https://doi.org/10.1016/0895-9811(94)90008-6.
Coira, B., Kay, S.M., 1993. Implications of Quaternary volcanism at Cerro Tuzgle for crustal and mantle evolution of the Puna Plateau, Central Andes, Argentina. Contrib. Mineral. Petrol. 113, 40–58. https://doi.org/10.1007/BF00320830.
Coira, B., 1995. Cerro tuzgle geothermal prospect, Jujuy, Argentina. Proceedings of the World Geothermal Congress, pp. 1161–1165.
Coira, B.L., 2008. Recursos Geotérmicos de Alta Entalpía De La Provincia de Jujuy, in: XVII Congreso Geológico Argentino. San Salvador de Jujuy, pp. 563–576.
Coutand, I., Cobbold, P.R., De Urreiztieta, M., Gautier, P., Chauvin, A., Gapais, D., Rossello, E.A., López-Gamundí, O., 2001. Style and history of Andean deformation, Puna plateau, northwestern Argentina. Tectonics 20, 210–234. https://doi.org/10.1029/2000TC900031.
CREGEN, 1988. Estudio Geotérmico Del área Tuzgle-Tocomar- Pompeya. Neuquén.
Crossey, L.J., Karlstrom, K.E., Springer, A.E., Newell, D., Hilton, D.R., Fischer, T., 2009. Degassing of mantle-derived CO2 and He from springs in the southern Colorado Plateau region—neotectonic connections and implications for groundwater systems. Geol. Soc. Am. Bull. 121 (7–8), 1034–1053.
Dapeña, C., Panarello, H., 2011. Composición isotópica de las precipitaciones en el Noroeste Argentino. VII Congreso Argentino de Hidrogeología y V Seminario Hispano-Latinoamericano Sobre Temas Actuales de la Hidrología Subterránea. Salta, Argentina, pp. 385–392.
D'Amore, F., Panichi, C., 1980. Evaluation of deep temperatures of hydrothermal systems by a new gas geothermometer. Geochem. Cosmochim. Acta 44, 549–556.
Del Papa, C., Hongn, F., Powell, J., Payrola, P., Do Campo, M., Strecker, M.R., Petrinovic, I., Schmitt, A.K., Pereyra, R., 2013. Middle Eocene-Oligocene broken-foreland evolution in the Andean Calchaqui Valley, NW Argentina: Insights from stratigraphic, structural and provenance studies. Basin Res. 25, 574–593. https://doi.org/10.1111/bre.12018.
Déruelle, B., 1991. Petrology of Quaternary shoshonitic lavas of northwestern Argentina. Geol. Soc. Am. Spec. Pap. 265, 201–216. https://doi.org/10.3758/BF03198973.
Elders, W.A., Moore, J.N., 2016. Geology of geothermal resources. Geothermal Power Generation: Developments and Innovation. Elsevier Ltd, pp. 7–32. https://doi.org/10.1016/B978-0-08-100337-4.00002-4.
Evans, W., White, L., Rapp, J., 1998. Geochemistry of some gases in hydrothermal fluids from the southern Juan de Fuca Ridge. J. Geophys. Res. 15, 305–313.
Facca, G., Tonani, F., 1967. The self-sealing geothermal field. Bull. Volcanol. 30, 271–273. https://doi.org/10.1007/BF02597674.
Faulds, J.E., Hinz, N.H., 2015. Favorable tectonic and structural settings of geothermal systems in the Great Basin Region, Western USA: proxies for discovering blind geothermal systems. World Geotherm. Congress 1–6, 2015.
Faulkner, D.R., Lewis, A.C., Rutter, E.H., 2003. On the internal structure and mechanics of large strike-slip fault zones: field observations of the Carboneras fault in southeastern Spain. Tectonophysics. https://doi.org/10.1016/S0040-1951(03)00134-3.
Faulkner, D.R., Armitage, P.J., 2013. The effect of tectonic environment on permeability development around faults and in the brittle crust. Earth Planet. Sci. Lett. 375, 71–77. https://doi.org/10.1016/j.epsl.2013.05.006.
Faulkner, D.R., Mitchell, T.M., Rutter, E.H., Cembrano, J., 2008. On the Structure and Mechanical Properties of Large Strike-Slip Faults 139–150. https://doi.org/10.1144/sp299.9, 299.
Faulkner, D.R., Jackson, C.A.L., Lunn, R.J., Schlische, R.W., Shipton, Z.K., Wibberley, C. A.J., Withjack, M.O., 2010. A review of recent developments concerning the structure, mechanics and fluid flow properties of fault zones. J. Struct. Geol. 32, 1557–1575. https://doi.org/10.1016/j.jsg.2010.06.009.
Fernandez-Turiel, J.L., Saavedra, J., Perez-Torrado, F.J., Rodriguez-Gonzalez, A., Rejas, M., Guillou, H., Aulinas, M., 2021. New ages, morphometric and geochemical data on recent shoshonitic volcanism of the Puna, Central Volcanic Zone of Andes: San Jerónimo and Negro de Chorrillos volcanoes. J. South Amer. Earth Sci. 109 https://doi.org/10.1016/j.jsames.2021.103270.
Filipovich, R.E., Barrios, A., Ahumada, M.F., Chiodi, A., Báez, W., Giordano, G., Viramonte, J.G., 2017. Probabilistic Assessment of Electrical Potential of Tocomar Geothermal Field (Central Puna - NW Argentina) Using Volumetric Method. 39th New Zealand Geothermal Workshop. University of Auckland, Rotorua, p. 84.
Filipovich, R., Báez, W., Groppelli, G., Ahumada, F., Aldega, L., Becchio, R., Berardi, G., Bigi, S., Caricchi, C., Chiodi, A., Corrado, S., De Astis, G., De Benedetti, A.A., Invernizzi, C., Norini, G., Soligo, M., Taviani, S., Viramonte, J.G., Giordano, G., 2020. Geological Map of the Tocomar Basin (Puna Plateau, NW Argentina). Implication for the geothermal system investigation. Energies 13, 5492. https://doi.org/10.3390/en13205492.
Fiorella, R.P., Poulsen, C.J., Zolá, R.S.P., Jeffery, M.L., Ehlers, T.A., 2015. Modern and long-term evaporation of central Andes surface waters suggests paleo archives underestimate Neogene elevations. Earth Planet. Sci. Lett. 432, 59–72.
García, M.G., Borda, L.G., Godfrey, L.V., Lopez Steinmetz, R.L., Losada-Calderon, A., 2020. Characterization of lithium cycling in the Salar De Olaroz, Central Andes, using a geochemical and isotopic approach. Chem. Geol. 531, 119340 https://doi.org/10.1016/j.chemgeo.2019.119340.

Garg, S.K., Combs, J., 2010. Appropriate use of USGS volumetric heat in place method and Monte Carlo calculations. Proceedings: Thirty-Fourth Workshop on Geothermal Reservoir Engineering. Stanford University, Stanford, California.
Garg, S.K., Combs, J., 2015. A reformulation of USGS volumetric 'heat in place' resource estimation method. Geothermics 55, 150–158. https://doi.org/10.1016/j.geothermics.2015.02.004.
Garzione, C.N., Hoke, G.D., Libarkin, J.C., Withers, S., MacFadden, B., Eiler, J., Ghosh, P., Mulch, A., 2008. Rise of the Andes. Science 320, 1304–1307. https://doi.org/10.1126/science.1148615.
Garzione, C.N., McQuarrie, N., Perez, N.D., Ehlers, T.A., Beck, S.L., Kar, N., Eichelberger, N., Chapman, A.D., Ward, K.M., Ducea, M.N., Lease, R.O., Poulsen, C. J., Wagner, L.S., Saylor, J.E., Zandt, G., Horton, B.K., 2017. Tectonic evolution of the Central Andean Plateau and implications for the growth of Plateaus. Annu. Rev. Earth Planet. Sci. 45, 529–559. https://doi.org/10.1146/annurev-earth-063016-020612.
Giggenbach, W., 1988. Geothermal solute equilibria, derivation of Na–K–Mg–Ca geoindicators. Geochim. Cosmochim. Acta 52, 2749–2765.
Giggenbach, W.F., 1991. Chemical techniques in geothermal exploration. Appl. Geochem. Geotherm. Reserv. Dev. 119–144.
Giggenbach, W.F., Goguel, R., 1989. Collection and Analysis of Geothermal and Volcanic Water and Gas Discharges. Chemistry Division. Department of Scientific and Industrial Research, Petone, New Zealand, p. 81. Unpublished Report.
Gilfillan, S.M.V., Sherwood Lollar, B., Holland, G., Blagburn, D., Stevens, S., Schoell, M., Cassidy, M., Ding, Z., Lacrampe-Couloume, G., Ballentine, C.J., 2009. Solubility trapping in formation water as dominant CO2 sink in natural gas fields. Nature 458, 614–618.
Giordano, G., Pinton, A., Cianfarra, P., Baez, W., Chiodi, A., Viramonte, J., Norini, G., Groppelli, G., 2013. Structural control on geothermal circulation in the Cerro Tuzgle-Tocomar geothermal volcanic area (Puna plateau, Argentina). J. Volcanol. Geotherm. Res. 249, 77–94. https://doi.org/10.1016/j.jvolgeores.2012.09.009.
Giordano, G., Ahumada, F., Aldega, L., Baez, W., Becchio, R., Bigi, S., Caricchi, C., Chiodi, A., Corrado, S., De Benedetti, A.A., Favetto, A., Filipovich, R., Fusari, A., Groppelli, G., Invernizzi, C., Maffucci, R., Norini, G., Pinton, A., Pomposiello, C., Tassi, F., Taviani, S., Viramonte, J., 2016. Preliminary data on the structure and potential of the tocomar geothermal field (Puna Plateau, Argentina). Energy Procedia 97, 202–209. https://doi.org/10.1016/j.egypro.2016.10.055.
Goff, F., Janik, C.J., 2000. Geothermal systems. Encyclopedia of Volcanoes 2000, pp. 817–834.
Gorustovich, S.A., Monaldi, C.R., Salfity, J.A., 2011. Geology and Metal Ore Deposits in the Argentine Puna, pp. 169–187.
Grant, M.A., 2014. Stored-heat assessments: a review in the light of field experience. Geotherm. Energy Sci. 2, 49–54. https://doi.org/10.5194/gtes-2-49-2014.
Grant, M.A., 2018. Stored heat and recovery factor reviewed. Proceedings: 43rd Workshop on Geothermal Reservoir Engineering. Stanford University, Stanford, California, pp. 1–8.
Gromoll, C., 2017. Petrophysical Characterization of Cap and Reservoir Rocks of the Tocomar geothermal System. NW-Argentina). Bochum University of Applied Sciences, Puna Plateau.
Heap, M.J., Gravley, D.M., Kennedy, B.M., Gilg, H.A., Bertolett, E., Barker, S.L.L., 2020. Quantifying the role of hydrothermal alteration in creating geothermal and epithermal mineral resources: The Ohakuri ignimbrite (Taupō Volcanic Zone, New Zealand). J. Volcanol. Geotherm. Res. 390 https://doi.org/10.1016/j.jvolgeores.2019.106703.
Hidroproyectos, S.A., Stec, S.R.L., Sepic, S.C., 1984. Estudio De La Segunda Fase De Prefactibilidad Geotérmica Del área denominada Tuzgle. Departamento de Susques, Provincia de Jujuy, Ministerio de Economía, Jujuy.
Hilton, D.R., Hammerschmidt, K., Teufel, S., Friedrichsen, H., 1993. Helium isotope characteristics of Andean geothermal fluids and lavas. Earth Planet. Sci. Lett. 120 (3–4), 265–282.
Hoke, L., Hilton, D.R., Lamb, S.H., Hammerschmidt, K., Friedrichsen, H., 1994. 3He evidence for a wide zone of active mantle melting beneath the Central Andes. Earth Planet. Sci. Lett. 128 (3–4), 341–355.
Hongn, F., del Papa, C., Powell, J., Petrinovic, I., Mon, R., Deraco, V., 2007. Middle Eocene deformation and sedimentation in the Puna-Eastern Cordillera transition (23°-26°S): control by preexisting heterogeneities on the pattern of initial Andean shortening. Geology 35, 271–274. https://doi.org/10.1130/G23189A.1.
Hongn, F., Mon, R., Petrinovic, I.A., del Papa, C., Powell, J., 2010. Inversión y reactivación tectónicas cretácico-cenozoicas en el noroeste argentino: Influencia de las heterogeneidades del basamento neoproterozoico-paleozoico inferior. Re. Asoc. Geol. Argentina.
Hudson-Edwards, K.A., Archer, J., 2012. Geochemistry of As-, F-and B-bearing waters in and around San Antonio de los Cobres, Argentina, and implications for drinking and irrigation water quality. J. Geochem. Explor. 112, 276–6284. https://doi.org/10.1016/j.gexplo.2011.09.007.
Ibarra, F., Prezzi, C.B., 2019. The thermo-mechanical state of the andes in the altiplano-puna region: Insights from curie isotherm and effective elastic thickness determination. Rev. Asoc. Geol. Argentina 76, 352–362.
Inguaggiato, S., Rizzo, A., 2004. Dissolved helium isotope ratios in ground-waters: a new technique based on gas–water re-equilibration and its application to Stromboli volcanic system. Appl. Geochem. 19 (5), 665–673.
Isacks, B.L., 1988. Uplift of the central Andean Plateau and bending of the Bolivian Orocline. J. Geophys. Res. 93, 3211–3231. https://doi.org/10.1029/JB093iB04p03211.
Jolie, E., Scott, S., Faulds, J., Chambefort, I., Axelsson, G., Gutiérrez-Negrín, L.C., Regenspurg, S., Ziegler, M., Ayling, B., Richter, A., Zemedkun, M.T., 2021. Geological controls on geothermal resources for power generation. Nat. Rev. Earth Environ. https://doi.org/10.1038/s43017-021-00154-y.
Jordan, T.E., Isacks, B.L., Allmendinger, R.W., Brewer, J.A., Ramos, V.A., Ando, C.J., 1983. Andean Tectonics Related to Geometry of Subducted Nazca Plate. Geological Society of America Bulletin https://doi.org/10.1130/0016-7606(1983)94<341:ATRTGO>2.0.CO;2.
Kay, S.M., Coira, B., Viramonte, J., 1994. Young mafic back arc volcanic rocks as indicators of continental lithospheric delamination beneath the Argentine Puna plateau, central Andes. J. Geophys. Res. 99 (B12), 24323–24339.
Koukharsky, M., Munizga, F., 1990. Los Volcanes Guanaquero, Chivinar, Tul Tul, Del Medio y Pocitos, Provincia de Salta. Litologia y Edades K/Ar, in. XI Congreso Geologico Argentino, San Juan, pp. 54–57.
Lanza, F., Tibaldi, A., Bonali, F.L., Corazzato, C., 2013. Space-time variations of stresses in the Miocene-Quaternary along the Calama-Olacapato-El Toro Fault Zone, Central Andes. Tectonophysics 593, 33–56. https://doi.org/10.1016/j.tecto.2013.02.029.
Lezaeta, P., Brasse, H., 2001. Electrical conductivity beneath the volcanoes of the NW Argentinian Puna. Geophys. Res. Lett. 28, 4651–4654. https://doi.org/10.1029/2001GL013582.
Lindsey, C.R., Ayling, B.F., Asato, G., Seggiaro, R., Carrizo, N., Larcher, N., Marquetti, C., Naón, V., Serra, A.C., Faulds, J.E., Coolbaugh, M.F., 2021. Play fairway analysis for geothermal exploration in north-western Argentina. Geothermics 95, 102128. https://doi.org/10.1016/j.geothermics.2021.102128.
López, D.L., Smith, L., 1995. Fluid flow in fault zones: analysis of the interplay of convective circulation and topographically driven groundwater flow. Water Resour. Res. 31, 1489–1503. https://doi.org/10.1029/95WR00422.
López, D.L., Bundschuh, J., Birkle, P., Armienta, M.A., Cumbal, L., Sracek, O., Cornejo, L., Ormachea, M., 2012. Arsenic in volcanic geothermal fluids of Latin America. Sci. Total Environ. 429, 57–75. https://doi.org/10.1016/j.scitotenv.2011.08.043.
Lucazeau, F., 2019. Analysis and mapping of an updated terrestrial heat flow data set. Geochem. Geophys. Geosyst. 20, 4001–4024. https://doi.org/10.1029/2019GC008389.
Mamyrin, B.A., Tolstikhin, I.N., 1984. Helium Isotopes in Nature. Elsevier, Amsterdam.
Marrett, R.A., Strecker, M.R., 2000. Response of intracontinental deformation in the central andes to late cenozoic reorganization of south American plate motions.
Marrett, R.A., Allmendinger, R.W., Alonso, R.N., Drake, R.E., 1994. Late Cenozoic tectonic evolution of the Puna Plateau and adjacent foreland, northwestern Argentine Andes. J. South Amer. Earth Sci. 7, 179–207. https://doi.org/10.1016/0895-9811(94)90007-8.
Matteini, M., Mazzuoli, R., Omarini, R., Cas, R., Maas, R., 2002. The geochemical variations of the upper cenozoic volcanism along the Calama – Olacapato – El Toro transversal fault system in central Andes (~ 24 B S): petrogenetic and geodynamic implications. Tectonophysics 345, 211–227.
Mitchell, T.M., Faulkner, D.R., 2012. Towards quantifying the matrix permeability of fault damage zones in low porosity rocks. Earth Planet. Sci. Lett. 339–340, 24–31. https://doi.org/10.1016/j.epsl.2012.05.014.
Moeck, I.S., 2014. Catalog of geothermal play types based on geologic controls. Renewable Sustainable Energy Rev. 37, 867–882. https://doi.org/10.1016/j.rser.2014.05.032.
Moya Ruiz, F., 1993. Hidroquímica de la cuenca del río San Antonio de los Cobres de la provincia de Salta, Argentina. Actas del XII Congreso Geológico Argentino y II Congreso de Explotación de Hidrocarburos, pp. 137–145.
Muffler, P., Cataldi, R., 1978. Methods for regional assessment of geothermal resources. Geothermics 7, 53–89.
Nathenson, M., 1975. Physical factors determining the fraction of stored energy recoverable from hydrothermal convection systems and conduction-dominated areas. Geol. Surv. Menlo Park, Calif.(USA).
Nicolli, H.B., Suriano, J.M., Peral, M.A.G., Ferpozzi, L.H., Baleani, O.A., 1989. Groundwater contamination with arsenic and other trace elements in an area of the Pampa, Province of Córdoba, Argentina. Environ. Geol. Water Sci. 14 (1), 3–16.
Nicolli, H.B., Bundschuh, J., Blanco, M.D.C., Tujchneider, O.C., Panarello, H.O., Dapeña, C., Rusansky, J.E., 2012. Arsenic and associated trace-elements in groundwater from the Chaco-Pampean plain, Argentina: results from 100 years of research. Sci. Total Environ. 429, 36–56. https://doi.org/10.1016/j.scitotenv.2012.04.048.
Norini, G., Baez, W., Becchio, R., Viramonte, J., Giordano, G., Arnosio, M., Pinton, A., Groppelli, G., 2013. The Calama-Olacapato-El Toro fault system in the Puna Plateau, Central Andes: geodynamic implications and stratovolcanoes emplacement. Tectonophysics 608, 1280–1297. https://doi.org/10.1016/j.tecto.2013.06.013.
Norini, G., Cogliati, S., Baez, W., Arnosio, M., Bustos, E., Viramonte, J., Groppelli, G., 2014. The geological and structural evolution of the Cerro Tuzgle Quaternary stratovolcano in the back-arc region of the Central Andes, Argentina. J. Volcanol. Geotherm. Res. 285, 214–228. https://doi.org/10.1016/j.jvolgeores.2014.08.023.
Nordstrom, D.K, McCleskey, R.B., Ball, J.W., 2001. Processes governing arsenic geochemistry in the thermal waters of Yellowstone National Park. USGS Workshop on Arsenic in the Environment, Denver.
Ohmoto, H., Goldhaber, M.B., 1997. Sulfur and carbon isotopes. In: Barnes, H.L. (Ed.), Geochemistry of Hydrothermal Ore Deposits. John Wiley & Sons, pp. 517–611.
Oncken, O., Hindle, D., Kley, J., Elger, K., Victor, P., Schemmann, K., 2006. Deformation of the Central Andean upper plate system — facts, fiction, and constraints for plateau models. Andes https://doi.org/10.1007/978-3-540-48684-8_1.
Panarello, H., Sierra, J.L., Pedro, G., 1990. Flow patterns at the Tuzgle-Tocomar geotermal system, Salta-Jujuy, Argentina. Geothermal Investigations with Isotopes and Geochemical Techniques in Latin America, pp. 57–76.

Panarello, H., Sierra, J., Pedro, I., 1993. Flow Patterns at the Tuzgle-Tocomar Geothermal system, Salta Jujuy, Argentina: An Isotopic and Geochemical Approach 57–75. IAEATechnical Document 641.
Pang, Z.H., Reed, M., 1998. Theoretical chemical thermometry on geothermal waters: problems and methods. Geochim. Cosmochim. Acta 62 (6), 1083–1091.
Pesce, A.H., 2010. Argentina Country Update 10, 24–29, 2010.
Paoli, H.P., 2003. Recursos Hídricos de la Puna, Valles y Bolsones Áridos del Noroeste Argentino. Aprovechamiento de los Recursos Hídricos Y Tecnología de Riego en el Altiplano Argentino. INTA, EEA Salta, p. 274.
Parkhurst, D.L., Appelo, C.A.J., 1999. User's guide to PHREEQC (version 2)-a computer program for speciation, batch-reaction, one-dimensional transport, and inverse geochemical calculations. U.S. Geol. Surv. Water Resour. Investig. Rep. 312, 99–4259.
Peralta Arnold, Y.P., Cabassi, J., Tassi, F., Caffe, P.J., Vaselli, O., 2017. Fluid geochemistry of a deep-seated geothermal resource in the Puna plateau (Jujuy Province, Argentina). J. Volcanol. Geotherm. Res. 338, 121–134.
Petrinovic, I.A., Colombo Piñol, F., 2006. Phreatomagmatic and phreatic eruptions in locally extensive settings of Southern Central Andes: The Tocomar Volcanic Centre (24°10′S-66°34′W), Argentina. J. Volcanol. Geotherm. Res. 158, 37–50. https://doi.org/10.1016/j.jvolgeores.2006.04.013.
Petrinovic, I.A., Mitjavila, J., Viramonte, J.G., Becchio, R., Arnosio, M., 1999. Descripción geoquímica y geocronológica de secuencias volcánicas neógenas de Trasarco, en el extremo oriental de la Cadena Volcánica Transversal del Quevar (Noroeste de Argentina). Acta Geol. Hispánica 34, 255–272.
Petrinovic, I.A., Arnosio, J.M., Alvarado, G.E., Guzmán, S., 2005. Erupciones freáticas sintectónicas en el campo geotérmico de Tocomar, Salta. Rev. Asoc. Geol. Argentina 60, 132–141.
Petrinovic, I.A., Riller, U., Brod, J.A., Alvarado, G., Arnosio, M., 2006. Bimodal volcanism in a tectonic transfer zone: Evidence for tectonically controlled magmatism in the southern Central Andes, NW Argentina. J. Volcanol. Geotherm. Res. 152, 240–252. https://doi.org/10.1016/j.jvolgeores.2005.10.008.
Petrinovic, I.A., Martí, J., Aguirre-Díaz, G.J., Guzmán, S., Geyer, A., Paz, N.S., 2010. The Cerro Aguas Calientes caldera, NW Argentina: An example of a tectonically controlled, polygenetic collapse caldera, and its regional significance. J. Volcanol. Geotherm. Res. 194, 15–26. https://doi.org/10.1016/j.jvolgeores.2010.04.012.
Poreda, R., Craig, H., 1989. Helium isotope ratios in circum-Pacific volcanic arcs. Nature 338 (6215), 473–478.
Poreda, R.J., Jeffrey, A.W.A., Kaplan, I.R., Craig, H., 1988. Magmatic helium in subduction-zone natural gases. Chem. Geol. 71 (1–3), 199–210.
Quinao, J.J., Zarrouk, S.J., 2014. A review of the volumetric stored-heat resource assessment: one method, different results. Proceedings New Zealand Geothermal Workshop.
Ramelow, J., Riller, U., Romer, R.L., Oncken, O., 2006. Kinematic link between episodic trapdoor collapse of the Negra Muerta Caldera and motion on the Olacapato-El Toro Fault Zone, southern central Andes. Int. J. Earth Sci. 95, 529–541. https://doi.org/10.1007/s00531-005-0042-x.
Ramsay, J.G., 1980. The crack–seal mechanism of rock deformation. Nature 284, 135–139.
Riller, U., Petrinovic, I.A., Ramelow, J., Strecker, M., Oncken, O., 2001. Late cenozoic tectonism, collapse caldera and plateau formation in the Central Andes. Earth Planet. Sci. Lett. 188, 299–311. https://doi.org/10.1016/S0012-821X(01)00333-8.
Robidoux, P., Rizzo, A.L., Aguilera, F., Aiuppa, A., Artale, M., Liuzzo, M., Zummo, F., 2020. Petrological and noble gas features of Lascar and Lastarria volcanoes (Chile): Inferences on plumbing systems and mantle characteristics. Lithos 370, 105615.
Rollinson, H., 1993. Using Geochemical Data. Longman, London, UK, p. 352.
Rossetti, F., Aldega, L., Tecce, F., Balsamo, F., Billi, A., Brilli, M., 2011. Fluid flow within the damage zone of the Boccheggiano extensional fault (Larderello-Travale geothermal field, central Italy): structures, alteration and implications for hydrothermal mineralization in extensional settings. Geol. Mag. 148 (4), 558–579.
Rowland, J.V., Sibson, R.H., 2004. Structural controls on hydrothermal flow in a segmented rift system, Taupo Volcanic Zone, New Zealand. Geofluids 4, 259–283. https://doi.org/10.1111/j.1468-8123.2004.00091.x.
Salado Paz, N., Petrinovic, I.A., Do Campo, M., Brod, J.A., Nieto, F., da Silva Souza, V., Wemmer, K., Payrola, P., Ventura, R., 2017. Mineralogy, structural control and age of the Incachule Sb epithermal veins, the Cerro Aguas Calientes collapse caldera, Central Puna. J. South Amer. Earth Sci. https://doi.org/10.1016/j.jsames.2017.07.002.
Salfity, J., 1985. Lineamientos Transversales al Rumbo Andino en el Noroeste Argentino. IV Congreso geologico Chileno.
Salvini, F., Billi, A., Wise, D.U., 1999. Strike-slip fault-propagation cleavage in carbonate rocks: the Mattinata Fault zone, southern Apennines, Italy. J. Struct. Geol. 21, 1731–1749. https://doi.org/10.1016/S0191-8141(99)00120-0.
Sanchez-Alfaro, P., Sielfeld, G., Campen, B.Van, Dobson, P., Fuentes, V., Reed, A., Palma-Behnke, R., Morata, D., 2015. Geothermal barriers, policies and economics in Chile - lessons for the Andes. Renew. Sustain. Energy Rev. 51, 1390–1401. https://doi.org/10.1016/j.rser.2015.07.001.
Sánchez, M.C., Salfity, J.A., 1999. La cuenca cámbrica del Grupo Mesón en el Noroeste Argentino: desarrollo estratigráfico y paleogeográfico. Acta Geol. Hispánica 34, 123–139.
Sanci, R., Panarello, H.O., Gozalvez, M.R., 2020. Environmental isotopes as tracers of mining activities and natural processes: A case study of San Antonio de los Cobres River Basin, Puna Argentina. J. Geochem. Explor. 213, 106517.
Sano, Y., Marty, B., 1995. Origin of carbon in fumarolic gases from island arcs. Chem. Geol. 119, 265–274 https://doi.org/10.1016/0009-2541 (94)00097-R.
Sanyal, S.K., 2005. Classification of geothermal systems - a possible scheme. Proc. 30th Workshop on Geothermal Reservoir Engineering, Stanford.
Schoell, M., 1980. The hydrogen and carbon isotopic composition of methane from natural gases of various origins. Geochim. Cosmochim. Acta 44, 649–661.
Schoell, M., 1988. Multiple origins of methane in the Earth. Chem. Geol. 71, 1–10.
Schurr, B., Asch, G., Rietbrock, A., Kind, R., Pardo, M., Heit, B., Monfret, T., 1999. Seismicity and average velocities beneath the Argentine Puna plateau. Geophys. Res. Lett. 26, 3025–3028. https://doi.org/10.1029/1999GL005385.
Schurr, B., Asch, G., Rietbrock, A., Trumbull, R., Haberland, C., 2003. Complex patterns of fluid and melt transport in the central Andean subduction zone revealed by attenuation tomography. Earth Planet. Sci. Lett. 215, 105–119. https://doi.org/10.1016/S0012-821X(03)00441-2.
Schwab, K., Lippolt, H., 1974. K-Ar mineral ages and late Cenozoic history of the Solar de Cauchari area (Argentina Puna). In: Gonzales-Ferra, O. (Ed.), Symposium on Andean and Antartic Volcanology Problems, pp. 698–714. Santiago de Chile.
Schwarz, G., Diaz, G.C., Krüger, D., Martinez, E., Massow, W., Rath, V., Viramonte, J., 1994. Crustal high conductivity zones in the Southern Central Andes. Tectonics of the Southern Central Andes, pp. 49–67 https://doi.org/10.1007/978-3-642-77353-2_3.
Seggiaro, R.E., 2006. Variaciones estructurales a lo Largo del lineamiento Calama-Olacapato-El Toro en el Noroeste Argentino. Actas Del XI Congreso Geologico Chileno. Antofagasta, pp. 337–340.
Seggiaro, R., Guzmán, S., Pereyra, R., Coppolecchia, M., Cegarra, M., 2016. Neotectónica y volcanismo monogenético cuaternario sobre el segmento central del lineamiento calama olacapato toro, no Argentino. Rev. Asoc. Geol. Argentina 73, 468–477.
Seggiaro, R.E., Guzmán, S.R., Apaza, F.D., 2017. Control estructural sobre el magmatismo en los alrededores de San Antonio de los Cobres, sector oriental de la Puna Central. In: Grosse, P. (Ed.), XX Congreso Geológico Argentino. Asociación Geológica Argentina, Tucumán, pp. 142–146.
Sibson, R., 1986. Earthquakes and rock deformation in Crustal Fault Zones. Annu. Rev. Earth Planet. Sci. 14, 149–175. https://doi.org/10.1146/annurev.earth.14.1.149.
Sibson, R.H., 1994. Crustal stress, faulting and fluid flow. Geol. Soc. Spec. Publ. 78, 69–84. https://doi.org/10.1144/GSL.SP.1994.078.01.07.
Sibson, R.H., 1996. Structural permeability of fluid-driven fault-fracture meshes. J. Struct. Geol. 18, 1031–1042. https://doi.org/10.1016/0191-8141(96)00032-6.
Silva, S.de, 1989. Altiplano-Puna volcanic complex of the central Andes. Geology 17, 1102–1106 https://doi.org/10.1130/0091-7613(1989)017<1102:APVCOT>2.3.CO;2.
SKM; Sinclair Knight Merz Limited, 2002. Resource Capacity Estimates for High Temperature Geothermal Systems in the Waikato Region. Auckland.
Sobel, E.R., Hilley, G.E., Strecker, M.R., 2003. Formation of internally drained contractional basins by aridity-limited bedrock incision. J. Geophys. Res. 108 https://doi.org/10.1029/2002JB001883.
Sobolev, S.V., Babeyko, A.Y., 2005. What drives orogeny in the Andes? Geology 33, 617–620. https://doi.org/10.1130/G21557.1.
Springer, M., Förster, A., 1998. Heat-flow density across the central Andean subduction zone. Tectonophysics 291, 123–139. https://doi.org/10.1016/S0040-1951(98)00035-3.
Stelling, P., Shevenell, L., Hinz, N., Coolbaugh, M., Melosh, G., Cumming, W., 2016. Geothermal systems in volcanic arcs: Volcanic characteristics and surface manifestations as indicators of geothermal potential and favorability worldwide. J. Volcanol. Geotherm. Res. 324, 57–72. https://doi.org/10.1016/j.jvolgeores.2016.05.018.
Strecker, M.R., Alonso, R.N., Bookhagen, B., Carrapa, B., Hilley, G.E., Sobel, E.R., Trauth, M.H., 2007. Tectonics and climate of the Southern Central Andes. Annu. Rev. Earth Planet. Sci. 35, 747–787. https://doi.org/10.1146/annurev.earth.35.031306.140158.
Strecker, M.R., Sobel, E.R., Hilley, G.E., Bookhagen, B., 2012. Structural, geomorphic, and depositional characteristics of contiguous and broken foreland basins: examples from the Eastern Flanks of the Central Andes in Bolivia and NW Argentina. Tecton. Sediment. Basins 508–521 https://doi.org/10.1002/9781444347166.ch25.
Suzaño, N., Becchio, R., Sola, A., Ortiz, A., Nieves, A., Quiroga, M., Fuentes, G., 2017. The role of magma mixing in the evolution of the Early Paleozoic calc-alkaline granitoid suites. Eastern magmatic belt, Puna, NW Argentina. J. South Amer. Earth Sci. 76, 25–46.
Tassara, A., 2005. Interaction between the Nazca and South American plates and formation of the Altiplano-Puna plateau: Review of a flexural analysis along the Andean margin (15°-34°S). Tectonophysics 399, 39–57. https://doi.org/10.1016/j.tecto.2004.12.014.
Tassi, F., Aguilera, F., Darrah, T., Vaselli, O., Capaccioni, B., Poreda, R.J., Huertas, A.D., 2010. Fluid geochemistry of hydrothermal systems in the Arica-Parinacota, Tarapacá and Antofagasta regions (northern Chile). J. Volcanol. Geotherm. Res. 192 (1–2), 1–15.
Tassi, F., Fiebig, J., Vaselli, O., Nocentini, M., 2012. Origins of methane discharging from volcanic-hydrothermal, geothermal and cold emissions in Italy. Chem. Geol. 310, 36–48.
Turner, J.C.M., 1960. Estratigrafía de la sierra de Santa Victoria y adyacencias. Boletín de la Academia Nacional de Ciencias de Córdoba 41 163–196.
Turner, J.C.M., 1964. Descripción Geológica de la Hoja 7c. Carta Geologico-Economica de la Republica Argentina, Nevado de Cachi, Provincia de Salta escala 1: 200.000.
Vaselli, O., Tassi, F., Montegrossi, G., Capaccioni, B., Giannini, L., 2006. Sampling and analysis of volcanic gases. Acta Volcanol. 18, 65–76.
Vieira, F., Hamza, V., 2019. Assessment of geothermal resources of South America - a new look. Int. J. Terrestrial Heat Flow Appl. 2, 46–57. https://doi.org/10.31214/ijthfa.v2i1.32.
Viggiano-Guerra, J.C., Gutiérrez-Negrín, L.C.A., 2005. The Geothermal System of Araró, Mexico, as an Independent System of Los Azufres, pp. 24–29.

Viramonte, J.G., Galliski, M.A., Saavedra, V.A., Aparicio, A., García-Cacho, G.L., Escorza, C.M., 1984. El Finivulcanismo Básico De La Depresión De Arizaro, Provincia De Salta. IX Congreso Geológico Argentino. Bariloche, pp. 234–251.

Warren, J.K., 2010. Evaporites through time: tectonic, climatic and eustatic controls in marine and nonmarine deposits. Earth Sci. Rev. 98 (3), 217–268. https://doi.org/10.1016/j.earscirev.2009.11.004.

Webster, J.G., Nordstrom, D.K., 2003. Geothermal arsenic. Arsenic in Groundwater. Springer, Boston, MA, pp. 101–125.

White, D.E., Williams, D.L., 1975. Assessment of Geothermal Resources of the United States, 1975. US Department of the Interior, Geological Survey.

Whitman, D., Isacks, B.L., Kay, S.M., 1996. Lithospheric structure and along-strike segmentation of the Central Andean Plateau: Seismic Q, magmatism, flexure, topography and tectonics. Tectonophysics 259, 29–40. https://doi.org/10.1016/0040-1951(95)00130-1.

Williams, C.F., 2014. Evaluating the volume method in the assessment. GRC Trans. 38, 967–974.

Williams, C.F., Reed, M.J., Mariner, R.H., DeAngelo, J., Galanis, S.P.J., 2008a. Assessment of Moderate-and High-Temperature Geothermal Resources of the United States: U.S. Geological Survey Fact Sheet 2008-3082. U.S. Geological Survey Fact Sheet 2008-3082 1–4.

Williams, C.F., Reed, M.J., Mariner, R.H., 2008b. A Review of Methods Applied by the U. S. Geological Survey in the Assessment of Identified Geothermal Resources 30.

Whiticar, M.J., 1999. Carbon and hydrogen isotope systematic of bacterial formation and oxidation of methane. Chem. Geol. 161, 291–314.

Yuan, X., Sobolev, S.V., Kind, R., Oncken, O., Bock, G., Asch, G., Schurr, B., Graeber, F., Rudloff, A., Hanka, W., Wylegalla, K., Tibi, R., Haberland, C., Rietbrock, A., Giese, P., Wigger, P., Röwer, P., Zandt, G., Beck, S., Wallace, T., Pardo, M., Comte, D., 2000. Subduction and collision processes in the Central Andes constrained by converted seismic phases. Nature 408, 958–961. https://doi.org/10.1038/35050073.

Zarrouk, S.J., Moon, H., 2014. Efficiency of geothermal power plants: a worldwide review. Geothermics 51, 142–153. https://doi.org/10.1016/j.geothermics.2013.11.001.